AN INVESTIGATION ON ELECTRICAL AND MAGNETIC PROPERTIES OF Mn$_{0.50}$Zn$_{0.50-x}$Cu$_x$Fe$_2$O$_4$ FERRITES
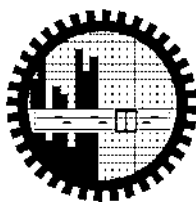
SUBMITTED

By

Md. Mahiuddin Talukder

A Dissertation Submitted to the Department of Physics, Bangladesh University of Engineering & Technology, Dhaka, in Partial Fulfillment of the Requirement for the Degree of Master of Philosophy in Physics

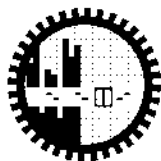**EXAMINATION ROLL NO.** : 100614008F
SESSION : October- 2006

DEPARTMENT OF PHYSICS

BANGLADESH UNIVERSITY OF ENGINEERING & TECHNOLOGY

DHAKA 1000, BANGLADESH

CANDIDATE'S DECLARATION

It is hereby declared that this thesis or any part of it has not been submitted elsewhere for the award of any degree or diploma.

—————————————————

MD. MAHIUDDIN TALUKDER

BANGLADESH UNIVERSITY OF ENGINEERING & TECHNOLOGY
DEPARTMENT OF PHYSICS, DHAKA 1000, BANGLADESH

CERTIFICATION OF THESIS

The thesis titled "**AN INVESTIGATION ON ELECTRICAL AND MAGNETIC PROPERTIES OF Mn$_{0.50}$Zn$_{0.50-x}$Cu$_x$Fe$_2$O$_4$ FERRITES**" submitted by **Md. Mahiuddin Talukder**, Roll No.: 100614008F, Session: October 2006, has been accepted as satisfactory in partial fulfillment of the requirement for the degree of **Master of Philosophy** in Physics on June 25, 2011.

BOARD OF EXAMINERS

1. (_____) Chairman
   Dr. A. K. M. Akther Hossain (Supervisor)
   Professor, Department of Physics,
   BUET, Dhaka-1000, Bangladesh

2. (_____) Member
   Head, Department of Physics, (Ex-Officio)
   BUET, Dhaka-1000, Bangladesh

3. (_____) Member
   Dr. Nazma Zaman,
   Professor, Department of Physics,
   BUET, Dhaka-1000, Bangladesh

4. (_____) Member
   Dr. A. B. M. Obaidul Islam, (External)
   Professor, Department of Physics,
   University of Dhaka, Dhaka-1000, Bangladesh.

DEDICATED TO
MY
BELOVED PARENTS
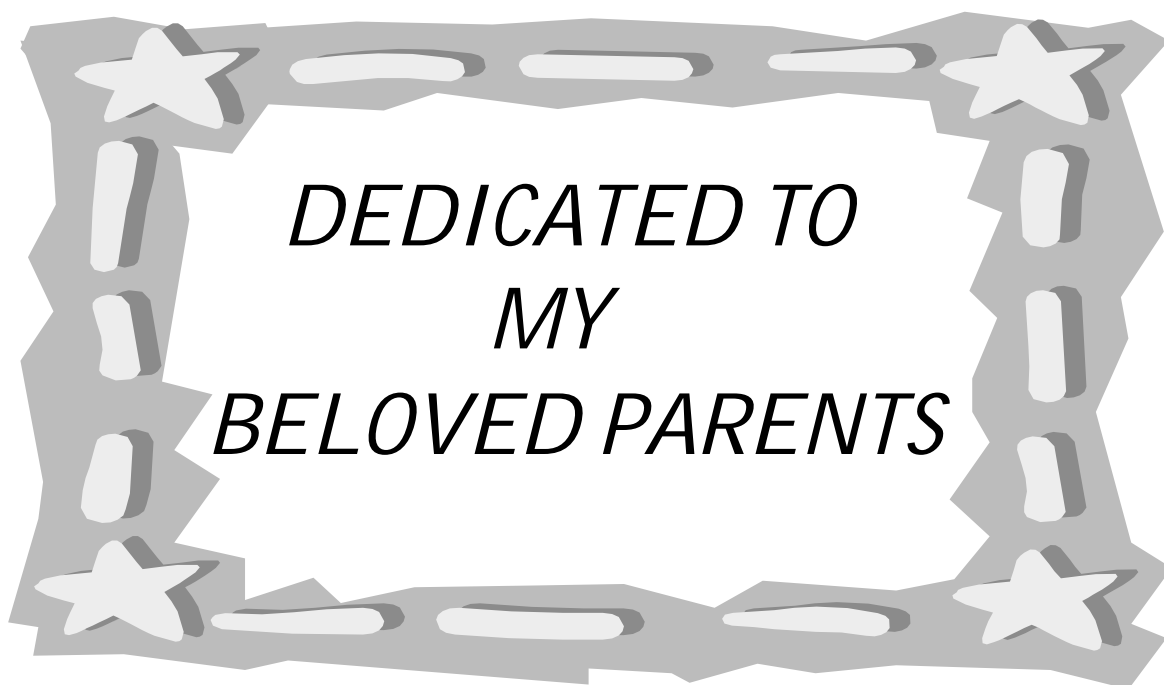
ABSTRACT

Polycrystalline $Mn_{0.50}Zn_{0.50-x}Cu_xFe_2O_4$ (with x = 0.00, 0.02, 0.05, 0.08, 0.10, 0.15, 0.20, 0.25, 0.30) ferrites are prepared by conventional solid state reaction technique. Pellet- and toroid-shaped samples are prepared from each composition and sintered at various temperatures (1200, 1250 and 1300°C) in air for 5 hours. Structural and surface morphology are studied by X-ray diffraction and optical microscopy. The AC magnetic properties of these ferrites are characterized by high frequency (1 kHz-100MHz) initial complex permeability and temperature dependent permeability measurements. DC magnetizations of all samples are measured by a SQUID magnetometer.

X-ray diffraction pattern show the formation of spinel crystal structure. Lattice parameters are found to decrease with substitution of Cu which can be explained with the help of ionic radii of substituted cations. The bulk density and the real part of the initial permeability, μ_i', of the samples increases with increasing Cu content up to x= 0.10. Beyond this value of x, there is a decrease of both density and μ_i'. The bulk density and μ_i' of the various polycrystalline $Mn_{0.50}Zn_{0.50-x}Cu_xFe_2O_4$ increases with increasing sintering temperature up to an optimum temperature (1250°C) above that they decrease. The average grain size increases with increasing Cu content. The μ_i' remain fairly constant in the frequency range up to some critical frequency characterized by the onset of resonance, while at higher frequency it drops rapidly to a very small value and imaginary part (μ_i'') increase to have a peak. The Néel temperature and the saturation magnetization of various compositions show an increasing trend as a function of composition due to strengthening of the *A-B* interaction. A possible correlation among sintering temperature, average grain size and density is also discussed.

CHAPTER 1

GENERAL INTRODUCTION

1.1 Introduction

There is an intense demand for high performance and miniaturization of many electronic devices. For some devices soft magnetic materials of high permeability is desired. Most modern soft ferrites have spinel type crystal structure. It has tetrahedral *A* site and octahedral *B* site in AB_2O_4 crystal structure (see 2.2). It shows various magnetic properties depending on the compositions and cation distribution. Various cations can be placed in *A* site and *B* site to tune its magnetic properties. Depending on *A* site and *B* site cations it can exhibit ferrimagnetic, antiferromagnetic, spin (cluster) glass and paramagnetic behaviour [1]. The general chemical formula of such ferrites is $MeFe_2O_4$, where *Me* represents one or several of the divalent transition metals. These types of ferrites are subjects of intense theoretical and experimental investigation due to their remarkable behaviour of magnetic and electric properties [2-12].

Mn-Zn ferrites are considered as one of the great importance of polycrystalline soft ferrite ceramic materials. This type of ceramics find extensive applications in electronic and telecommunication industry such as fabrication of transformers, frequency filters, magnetic recording heads, voice coil motors of computer hard disc drives etc. [2-3].This is due to their excellent properties such as high saturation magnetization, high initial permeability, high resistively and low losses. The essential feature of these materials is

the coexistence of high magnetization and high electric resistively. Therefore the replacement of these materials in near future will be questionable [4].

Many Researchers also showed their interest to investigate Cu-Zn ferrite [5-7]. Ni-Cu-Zn ferrite was extensively studied by various scientists because of their interesting characteristics in structural, electrical and magnetic properties [8-10]. Guan-Feng *et al.*[11] studied Mn-Zn-Cu ferrite while Mn is substituted in place of Zn. However no reports have been found for Cu substituted Mn-Zn ferrite. In the present research, structural and magnetic properties of various $Mn_{0.5}Zn_{0.5-x}Cu_xFe_2O_4$ ferrites prepared by solid state reaction technique will be investigated.

1.2 Objectives of the Present Work

The main objectives of the present research are as follows:

- Preparation of various $Mn_{0.5}Zn_{0.5-x}Cu_xFe_2O_4$ (for various x) samples.

- Perform structural characterizations, density and porosity of the samples.

- Study of surface morphology (grain size).

- Determination of ferrimagnetic to paramagnetic transition temperature (T_N) from temperature dependent initial permeability.

- Initial permeability as a function of frequency (1 kHz-120MHz) for samples having various microstructures (e. g. grain size).

- Measurement of DC magnetization

1.3 Summary of the Thesis

The thesis consists of following chapters:

Chapter 1 deals with the importance of ferrites and objectives of the present work.

Chapter 2 gives a brief overview of the materials, theoretical background as well as crystal structure of the spinel ferrites.

Chapter 3 gives the details of the sample preparation

Chapter 4 gives descriptions of different experimental setup that have been used in this research work.

Chapter 5 is devoted to the results of various investigations of the study and a brief discussion.

The conclusions drawn from the overall experimental results and discussion are presented in Chapter 6.

References

[1]   Hossain, A. K. M. A; Seki, M.; Kawai, T.; Tabata, H. "Colossal magnetoresistance in spinel type $Zn_{1-x}Ni_xFe_2O_4$," *J. Appl. Phys.*, **96**, 1273 (2004).

[2]   Sugimoto, M., "The past, present and future of ferrites," J. Am. Ceram. Soc., Vol-82, pp269-280, 1999.

[3]   Mangalaraja, R. V., Ananthakmar ,S. Manohar, P., Gnanam, F. D., Awano, M., "Characterisation of $Mn_{0.8}Zn_{0.2}Fe_2O_4$ synthesized by flash combustion technique," Mater. Sci. Eng. A, **367**, 301-305 (2004).

[4]   Rozman,M., Drofenik, M., "Sintering of nanosized MnZn ferrite powders," J. Am. Ceram. Soc.,
          81[7] (1998) 1757-1764.

[5]   Ahmed, M.A., Khalil, A.A.I., Solyman, S., "Laser induced structural and transport properties
          change in Cu-Zn ferrites" Journal of materials science, , Vol- 42, pp. 4098-4109 , 2007

[6]   Sattar, A. A., Rahman, S. A., "Dielectric Properties of Rare Earth Substituted Cu–Zn Ferrites",
          Phys. Stat. Sol. (a), Vol- 200, No. 2, pp 415–422, 2003.

[7]   Patil ,V. U. and Kulkarni, R. G., **"**Magnetic properties of Cu-Zn ferrite investigated by Mössbauer
          spectroscopy", Solid State Communications. Vol- 31, Issue 8, pp 551-555, 1979

[8]   Kim, C. S., Kim, W. C., An, S. Y., Lee, S. W., "Structure and mossbauer studies of Cu-dopped
          NiZn ferrites," *J. Magn. Magn. Mater.*, **213**, 215-216 (2000).

[9]   Nakamura, T.,"Low temperature sintering of Ni-Zn-Cu ferrire and its permeability spectra," *J.
          Magn. Magn. Mater.*, **168**, 285.(1997).

[10]   Yue, Z., Zhou, J., Gui, Z. and Li, L., Magnetic and electrical properties of low-temperature
          sintered Mn-doped NiCuZn ferrites, *J. Magn. Magn. Mater.*,pp 258-263, 2003

[11]   Guan-Feng, W., Bao-Feng, Z., Hong-E, Z., Xiao-Hui, D., Structure and Magnetic Properties of
          $Mn_xZn_{1-x}Cu_{0.2}Fe_{1.8}O_4$ Ferrite Nanoparticles Synthesized by Sol-Gel Auto-combustion, Journal of
          Inorganic Materials, Vol. 22, No. 6 Nov., 2007

CHAPTER 2

LITERATURE REVIEW

Double oxides of iron and other metals are important members of ferrimagnetic system commonly known as ferrites. The outstanding properties of ferrites are their complex magnetic structure, which can be varied to tailor their magnetic properties for various high frequency applications. In this chapter we describe a brief overview of the ferrites. The basic issue of ferrimagnetisms, crystal structure of the spinel ferrites and effect of non-magnetic Zn substitution by magnetic Cu on the magnetic moments in spinel ferrites are discussed. A few theoretical aspects of complex permeability are also discussed.

2.1 Overview of the materials

Ferrites commonly expressed by the general chemical formula $MeO.Fe_2O_3$, where Me represents divalent metals, first commanded the public attention when Hilpert (1909) focused on the usefulness of ferrites at high frequency [1]. A systematic investigation was launched by Snoek (1936) at Philips Research Laboratory [2]. At the same time Takai (1937) in Japan was seriously engaged in the research work on the same materials [1]. Snoek's extensive works on ferrites unveiled many mysteries regarding magnetic properties of ferrites. He was particularly looking for high permeability materials of cubic structure. This particular structure for symmetry reasons supports low crystalline anisotropy. He found suitable materials in the form of mixed spinels of the type $MeZnFe_2O_4$, where Me stands for metals like Cu, Mg, Ni, Co or Mn, for which permeability were found to be up to 4000 [1-2].

Caltun [3] studied magnetic properties of high frequency Ni-Zn ferrites doped with CuO. Upon increasing the Cu substitution, the average grain size decreases and the microstructure becomes more uniform with fewer pores. Initial permeability was higher

for higher Cu content. Chul Sung Kim [4] studied the structure of Cu-doped NiZn ferrite. The Lattice parameter increases linearly with Cu content.

Rahman [5] studied on Ni-Cu-Zn based ferrites. Average crystallite size increase linearly with calcined temperature. The lattice parameter and the ionic radius of the octahedral sites increase with copper content. The saturation magnetization decreases with increasing non-magnetic Cu content. Woo Chul Kim [6] studied growth of ultra fine NiCuZn ferrite and magnetic properties by sol-gel method. The saturation magnetization increases drastically with annealing temperature.

Nakamura [7] reported on low temperature sintering Ni-Cu-Zn ferrite and its permeability spectra. The complex permeability of the sintering ferrites is described as the summation of the spin rotational contribution and domain wall motion component. The permeability in 100MHz region is determined mainly by the spin rotation magnetization mechanism and it depends only on the post sintering density. The effect of domain wall contribution cannot be ignored in the 10MHz region. The domain wall contribution can be controlled not only by the post sintering density but also by the ferrites grain size.

Many Researchers studied Mn-Zn ferrites [8-9] and found the strong effect on their properties of composition, reactants, forming techniques and conditions of sintering for Mn-Zn ferrite.

There are two mechanisms in the phenomenon of permeability; spin rotation in the magnetic domains and wall displacements. The uncertainty of contribution from each of the mechanisms makes the interpretation of the experimental results difficult. Globus

[10] shows that the intrinsic rotational permeability μ_r and 180^0 wall permeability μ_w may be written as: $\mu_r = 1 + 2\pi M_s^2 / K$ and $\mu_w = 1 + 3\pi M_s^2 D / 4\gamma$, where M_s is the saturation magnetization, K is the total anisotropy, D is the grain diameter and $\gamma \equiv K\delta_w$ is the wall energy.

2.2 Magnetic ordering

The onset of magnetic order in solids has two basic requirements:

(i) Individual atoms should have magnetic moments (spins),

(ii) Exchange interactions should exist that couple them together.

Magnetic moments originate in solids as a consequence of overlapping of the electronic wave function with those of neighboring atoms. This condition is best fulfilled by some transition metals and rare-earths. The exchange interactions depend sensitively upon the inter-atomic distance and the nature of the chemical bonds, particularly of nearest neighbour atoms. When the positive exchange dominates, which corresponds to parallel coupling of neighbouring atomic moments (spins), the magnetic system becomes ferromagnetic below a certain temperature T_C called the Curie temperature. The common spin directions are determined by the minimum of magneto-crystalline anisotropy energy of the crystal. Therefore, ferromagnetic substances are characterized by spontaneous magnetization. But a ferromagnetic material in the demagnetized state displays no net magnetization in zero field because in the demagnetized state a ferromagnetic of macroscopic size is divided into a number of small regions called domains, spontaneously magnetized to saturation value and the directions of these spontaneous magnetization of the various domains are such that the net magnetization of the specimen is zero. The existence of domains is a consequence of energy minimization. The size and formation of

these domains is in a complicated manner dependent on the shape of the specimen as well as its magnetic and thermal history. When negative exchange dominates, adjacent atomic moments (spins) align antiparallel to each other, and the substance is said to be anti-ferromagnetic below a characteristic temperature, T_N, called the Néel temperature. In the simplest case, the lattice of an anti-ferromagnet is divided into two sublattices with the magnetic moments of these in anti-parallel alignment. This result is zero net magnetization.
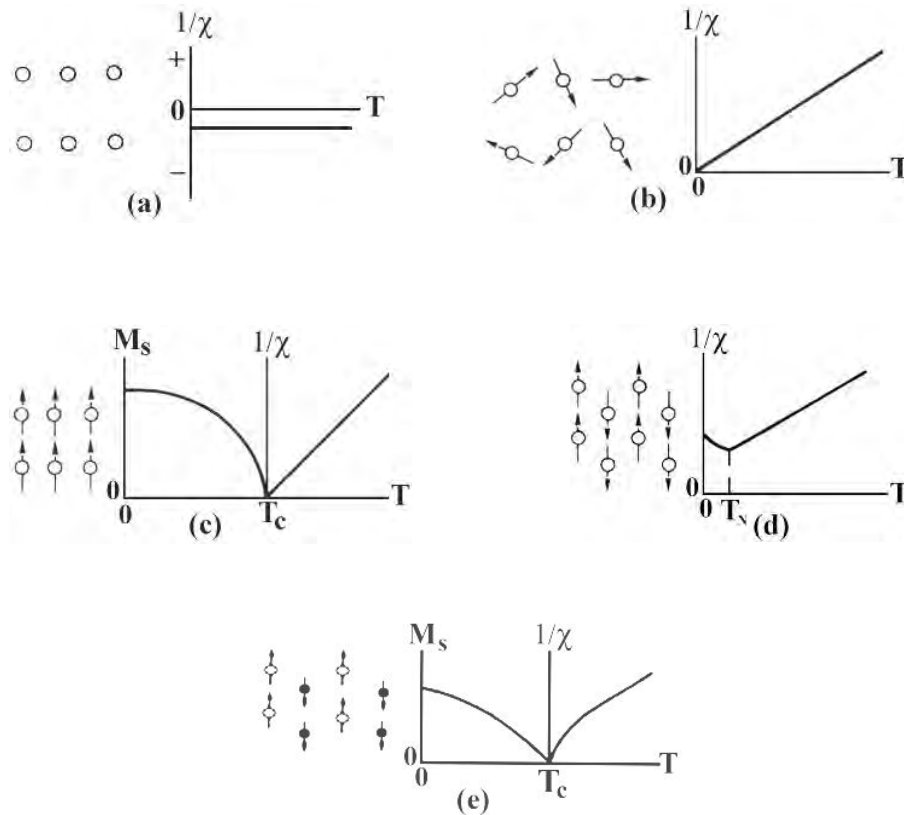

Figure 2.1. Temperature dependence of the inverse susceptibility for: (a) a diamagnetic material; (b) a paramagnetic material, showing Curie's law behaviour; (c) a ferromagnetic material, showing a spontaneous magnetization for $T<T_C$ and Curie-Weiss behaviour for $T>T_C$; (d) an antiferromagnetic material; (e) a ferrimagnetic material, showing a net spontaneous magnetization for $T<T_C$ and non linear behaviour for $T>T_C$.

A special case of anti-ferromagnetism is ferrimagnetism. In ferrimagnetism, there are also two sublattices with magnetic moments in opposite directions, but the magnetization of the sublattices are of unequal strength resulting in a non-zero magnetization and therefore has net spontaneous magnetization. At the macroscopic level of domain structures, ferromagnetic and ferrimagnetic materials are therefore similar.

The Curie and Néel temperatures characterize a phase transition between the magnetically ordered and disordered (paramagnetic) states. From these simple cases of magnetic ordering various types of magnetic order exists, particularly in metallic substances. Because of long-range order and oscillatory nature of the exchange interaction, mediated by the conduction electrons, structures like helical, conical and modulated patterns might occur. A useful property for characterizing the magnetic materials is the magnetic susceptibility, χ, defined as the magnetization, M, divided by the applied magnetic field, H i.e. $\chi = M / H$. The temperature dependence of susceptibility or more accurately, inverse of susceptibility is a good characterization parameter for magnetic materials; Fig. 2.1(e) shows that in the paramagnetic region, the variation of the inverse susceptibility with temperature of a ferrite material is decidedly non-linear. Thus the ferrite materials do not obey the Curie-Weiss law, $\chi = C /(T - T_C)$ [2,11].

2.3 Crystal structure of spinel ferrites

Ferrites have the cubic structure, which is very close to that of the mineral spinel $MgO.Al_2O_3$, and are called cubic spinel. Analogous to the mineral spinel, magnetic spinel have the general formula $MeO.Fe_2O_3$ or $MeFe_2O_4$ where Me is the divalent metal ion [12]. This crystal structure was first determined by Bragg and by Nishikawa [1,11].

Formerly, spinels containing *Fe* were called ferrites but now the term has been broadened to include many other ferrimagnets including garnets and hexagonal ferrites these need not necessarily contain iron. The spinel lattice is composed of a close-packed oxygen (radius about 1.3Å) arrangement in which 32 oxygen ions form a unit cell that is the smallest repeating unit in the crystal network. The unit cell of the ideal spinel structures is given in Fig. 2.2. Between the layers of oxygen ions, if we simply visualize them as spheres, there are interstices that may accommodate the metal ions (radii ranging from 0.6 to 0.8Å). Now, the interstices are not all the same: some which we call A sites are surrounded by or coordinated with 4 nearest neighboring oxygen ions whose lines connecting their centers form a tetrahedron. Thus, *A* sites are called tetrahedral sites. The other type of sites (*B* sites) is coordinated by 6 nearest neighbor oxygen ions whose center connecting lines describe an octahedron. The *B* sites are called octahedral sites. In the unit cell of 32 oxygen ions there are 64 tetrahedral sites and 32 octahedral sites. If all these were filled with metal ions, of either +2 or +3 valence, the positive charge would be very much greater than the negative charge and so the structure would not be electrically neutral.

It turns out that of the 64 tetrahedral sites, only 8 are occupied and out of 32 octahedral sites, only 16 are occupied. Thus the unit cell contains eight formula units AB_2O_4, with 8 *A* sites, 16 *B* sites and 32 oxygen ions, and total of   8 x 7 = 56 ions. A spinel unit cell contains two types of subcells, Fig. 2.2. The two types of subcells alternate in a three-dimensional array so that each fully repeating unit cell requires eight subcells, Fig. 2.3.
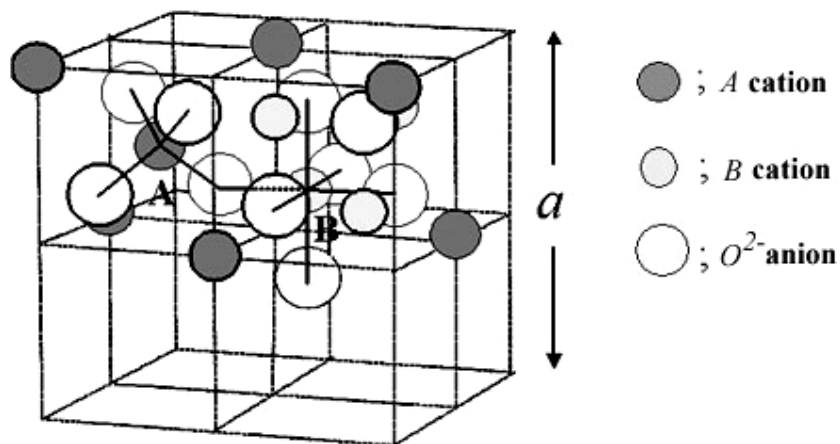
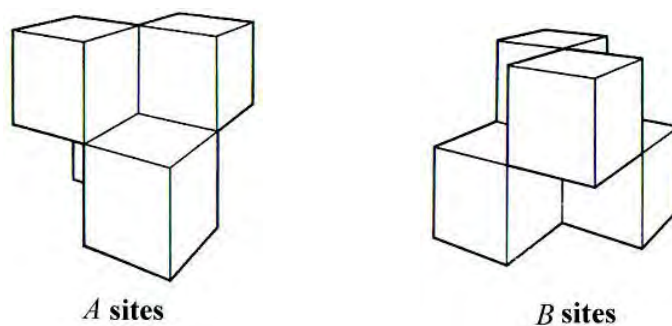**Figure 2.2.** Two subcells of a unit cell of the spinel structure.

Figure 2.3. Unit cell of spinel ferrite divided into eight subcells with *A* and *B* sites.

The positions of the ions in the spinel lattice are not perfectly regular (as the packing of hard spheres) and some distortion does occur. The tetrahedral sites are often too small for the metal ions so that the oxygen ions move slightly to

accommodate them. The oxygen ions connected with the octahedral sites move in such a way as to shrink the size the octahedral cell by the same amount as the tetrahedral site expands. The movement of the tetrahedral oxygen is reflected in a quantity called the oxygen parameter, which is the distance between the oxygen ion and the face of the cube edge along the cube diagonal of the spinel subcell. This distance is theoretically equal to $3/8a_0$ where a_0 is the lattice constant [1].

2.4 Cation distribution of spinel ferrites

In spinel structure the distribution of cations over the tetrahedral or *A* sites and octahedral or *B* sites can be present in a variety of ways. If all the Me^{2+} ions in $Me^{2+}Me_2^{3+}O_4$ are in tetrahedral and all Me^{3+} ions in octahedral positions, the spinel is then called normal spinel. Another cation distribution in spinel exists, where one half of the cations Me^{3+} are in the *A* positions and the rest, together with the Me^{2+} ions are randomly distributed among the *B* positions. The spinel having the latter kind of cation distribution is known as inverse spinel. The distribution of these spinels can be summarized as [2, 13-14]:

1) Normal spinels, i.e. the divalent metal ions are on *A*-sites: $Me^{2+}[Me_2^{3+}]O_4$,

2) Inverse spinels, i.e. the divalent metal ions are on *B*-sites: $Me^{3+}[Me^{2+}Me_2^{3+}]O_4$.

A completely normal or inverse spinel represents the extreme cases. *Zn* ferrites have normal spinel structure and its formula may be written as $Zn^{2+}[Fe^{3+}Fe^{3+}]O_4^{2-}$. On the other hand, *Ni* ferrites have inverse spinel structure and its formula may be written as $Fe^{3+}[Ni^{2+}Fe^{3+}]O_4^{2-}$. There are many spinel oxides which have cation distributions intermediate between these two extreme cases and are called mixed spinels. The general cation distribution for the spinel can be indicated as:

$$(Me_x^{2+}Me_{1-x}^{3+})[Me_{1-x}^{2+}Me_{1+x}^{3+}]O_4$$
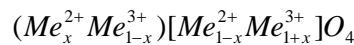
where the first and third brackets represent the A and B sites respectively. For normal spinel $x = 1$, for inverse spinel $x = 0$. The quantity x is a measure of the degree of inversion. In the case of some spinel oxides x depends upon the method of preparation.

2.5 Interaction between magnetic moments on lattice sites

Spontaneous magnetization of spinels (at 0K) can be estimated on the basis of their composition, cation distribution, and the relative strength of the possible interaction. Since cation-cation distances are generally large, direct (ferromagnetic) interactions are negligible. Because of the geometry of orbital involved, the strongest superexchange interaction is expected to occur between octahedral and tetrahedral cations. The strength of interaction or exchange force between the moments of the two metal ions on different sites depends on the distances between these ions and the oxygen ion that links them and also on the angle between the three ions. The nearest neighbours of a tetrahedral, an octahedral and an anion site are shown in Fig. 2.4. The interaction is greatest for an angle of 180^0 and also where the interionic distances are the shortest.
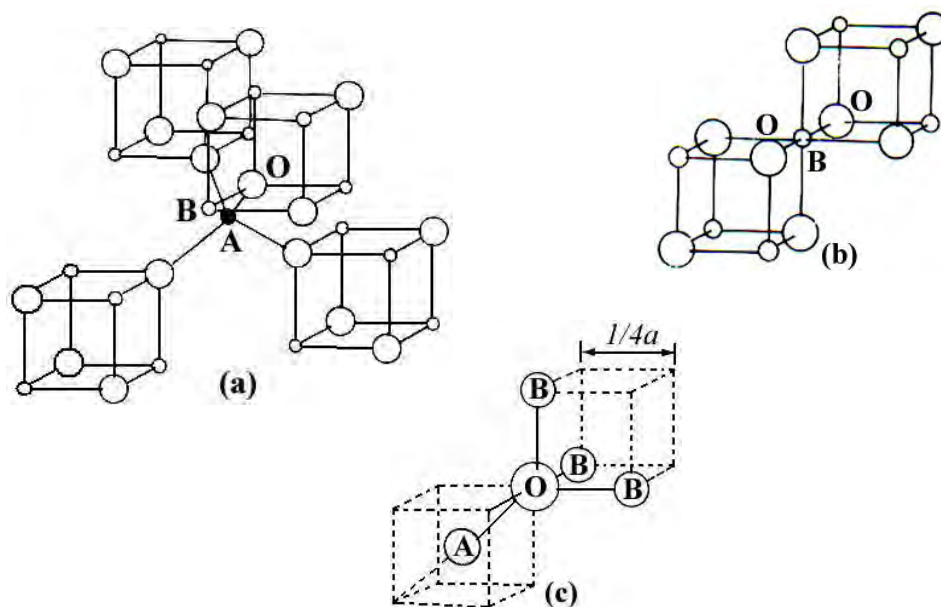

Figure 2.4. Nearest neighbours of (a) a tetrahedral site, (b) an octahedral site and (c) an anion site.

Fig. 2.5 shows the inteionic distances and the angles between the ions for the different type of interactions. In the *A-A* and *B-B* cases, the angles are too small or the

distances between the metal ions and the oxygen ions are too large. The best combination of distances and angles are found in *A-B* interactions.
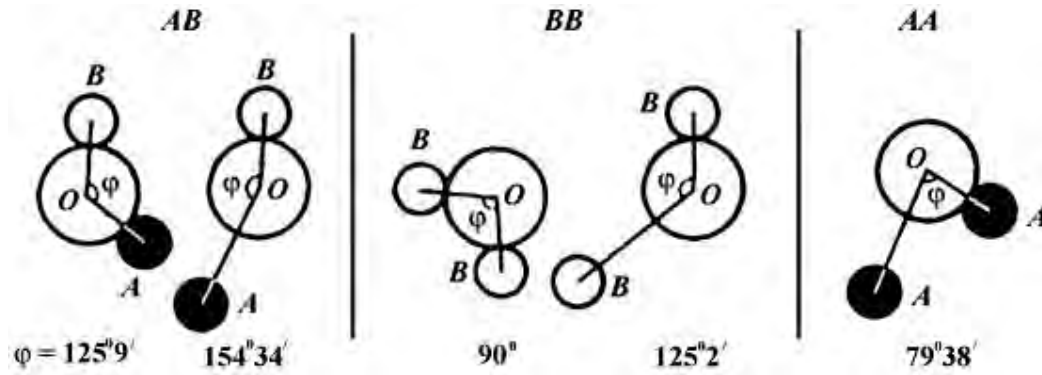

Figure 2.5. Interionic angles in the spinel structure for the different type of lattice site interactions.

For an undistorted spinel, the *A-O-B* angles are about 125^0 and 154^0 [1-2, 15]. The *B-O-B* angles are 90^0 and 125^0 but the latter, one of the *B-B* distances is large. In the *A-A* case the angle is about 80^0. Therefore, the interaction between moments on the *A* and *B* site is strongest. The *BB* interaction is much weaker and the most unfavorable situation occurs in the *AA* interaction. By examining the interaction involving the major contributor, or the *A-B* interaction which orients the unpaired spins of these ions antiparallel, Néel was able to explain the ferrimagnetism of ferrites.

2.6 Magnetism in spinel ferrite

The magnetic moment of a free atom is associated with the orbital and spin motions of electrons in an incomplete sub-shell of the electronic structure of the atom. In crystals the orbital motions are quenched, that is the orbital planes may be considered to be fixed in space relative to the crystal lattice, and in such a way that in bulk the crystal has no resultant moment from this source. Moreover this orbital-lattice coupling is so strong that the

application of a magnetic field has little effect upon it. The spin axes are not tightly bound to the lattice as are the orbital axes. The anions surrounding a magnetic cation subject it to a strong inhomogeneous electric field and influence the orbital angular momentum. However, the spin angular momentum remains unaffected. For the first transition group elements this crystal field effect is intense partly due to the large radius of the 3d shell and partly due to the lack of any outer electronic shell to screen the 3d shell whose unpaired electrons only contribute to the magnetic moment. We have originally defined the magnetic moment in connection with permanent magnets. The electron itself may well be called the smallest permanent magnet [1]. For an atom with a resultant spin quantum number S, the spin magnetic moment will be

$$\mu = g\sqrt{S(S+1)}\mu_B$$

where g is the Landé splitting factor and μ_B, known as the Bohr magneton, is the fundamental unit of magnetic moment. The value of g for pure spin moment is 2 and the quantum number associated with each electron spin is $\pm 1/2$. The direction of the moment is comparable to the direction of the magnetization (from South to North poles) of a permanent magnet to which the electron is equivalent. Fig. 2.6 illustrates the electronic configuration of Fe atoms and Fe^{3+} ions. Fe atom has four unpaired electrons and Fe^{3+} ion has five unpaired electrons. Each unpaired electron spins produced 1 Bohr magneton. In compounds, ions and molecules, account must be taken of the electrons used for bonding or transferred in ionization. It is the number of unpaired electrons remaining after these processes occur that gives the net magnetic moment [1]. According to the Hund's rules the moment of Fe atom and Fe^{3+} ion are $4\mu_B$ and $5\mu_B$ respectively. Similarly the moment of Fe^{2+} and Ni^{2+} ion are $4\mu_B$ and $3\mu_B$ respectively.
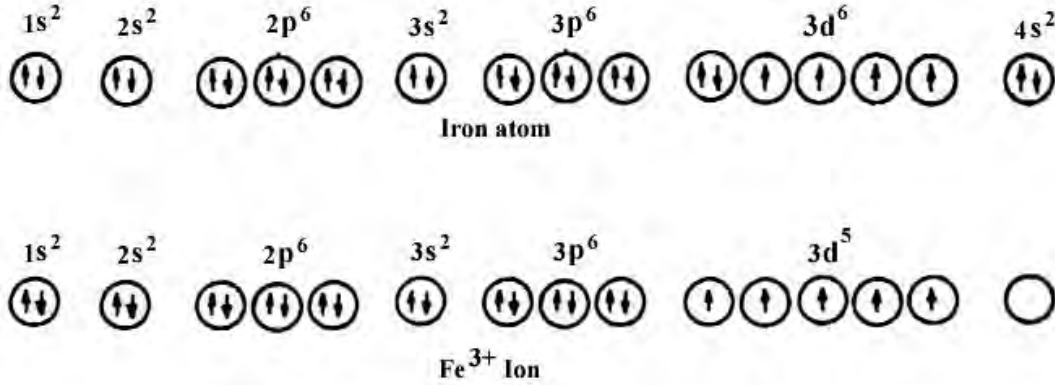
Figure 2.6. Electronic configuration of atoms and ions

2.6.1   Exchange interactions in spinel

The intense short-range electrostatic field, which is responsible for the magnetic ordering, is the exchange force that is quantum mechanical in origin and is related to the overlapping of total wave functions of the neighbouring atoms. The total wave function consists of the orbital and spin motions. Usually the net quantum number is written as *S*, because the magnetic moments arise mostly due to the spin motion as described above. The exchange interactions coupling the spins of a pair of electrons are proportional to the scalar product of their spin vectors [12, 14, 16],

$$V_{ij} = -2J_{ij}\vec{S}_i.\vec{S}_j \tag{2.1}$$

where J_{ij} is the exchange integral given in a self explanatory notation by

$$J_{ij} = \int \psi_i^*(1)\psi_j^*(2)\left[\frac{1}{r_{12}} + \frac{1}{r_{ij}} - \frac{1}{r_{i1}} - \frac{1}{r_{j2}}\right]\psi_i(1)\psi_j(2)dv_1 dv_2 \tag{2.2}$$

In this expression *r* 's are the distances, subscripts *i* and *j* refer to the atoms, 1 and 2 refers to the two electrons. If the *J* in equation (2.1) is positive, we achieve ferromagnetism. A negative *J* may give rise to anti-ferromagnetism or ferrimagnetism.

Magnetic interactions in spinel ferrites as well as in some ionic compounds are different from the one considered above because the cations are mutually separated by bigger anions (oxygen ions). These anions obscure the direct overlapping of the cation charge distributions, sometimes partially and some times completely making the direct exchange interaction very weak. Cations are too far apart in most oxides for a direct cation-cation interaction. Instead, superexchange interactions appear, i.e., indirect exchange via anion *p*-orbitals that may be strong enough to order the magnetic moments. Apart from the electronic structure of cations this type of interactions strongly depends on the geometry of arrangement of the two interacting cations and the intervening anion. Both the distance and the angles are relevant. Usually only the interactions with in first coordination sphere (when both the cations are in contact with the anion) are important. In the Neél theory of ferrimagnetism the interactions taken as effective are inter- and intra-sublattice interactions *A-B*, *A-A* and *B-B*. The type of magnetic order depends on their relative strength.

The superexchange mechanism between cations that operate via the intermediate anions was proposed by Kramer for such cases and was developed by Anderson and Van Vleck [13, 14]. A simple example of superexchange is provided by *MnO* which was chosen by Anderson. From the crystal structure of *MnO* it will be seen that the antiparallel manganese ions are collinear with their neighbouring oxygen ions. The O^{2-} ions each have six *2p* electrons in three antiparallel pairs. The outer electrons of the Mn^{2+} ions are in *3d* sub-shells which are half filled with five electrons in each. The phenomenon of superexchange is considered to be due to an overlap between the manganese 3*d* orbits and the oxygen 2*p* orbits with a continuous interchange of electrons between them. It appears that, for the overall energy of the system to be a minimum, the moments of the manganese ions on either side of the oxygen ion must be antiparallel. The manganese magnetic moments

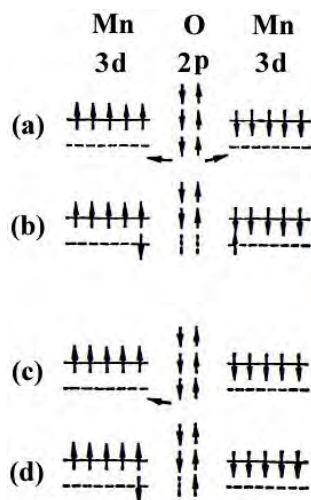are thus, in effect, coupled through the intervening oxygen ion. The idea is illustrated in Fig. 2.7.

Figure 2.7. Illustrating superexchange in *MnO*.

In Figs. 2.7(a) and 2.7(c) the outer electrons in a pair of Mn^{2+} ions, and in an intervening O^{2-} ion in the unexcited state, are shown by the arrows. One suggested mode of coupling is indicated in Fig. 2.7(b). The two electrons of a pair in the oxygen ion are simultaneously transferred, one to the left and the other to the right. If their directions of spin are unchanged then, by Hund's rules, the moments of the two manganese ions must be antiparallel as shown. Another possibility is represented in Fig. 2.7(d). One electron only has been transferred to the manganese ion on the left. The oxygen ion now has a moment of $1\mu_B$ and if there is negative interaction between the oxygen ion and the right-hand manganese ion then again the moments of the manganese ions will be antiparallel. If these ideas are accepted then the oxygen ions play an essential part in producing antiferromagnetism in the oxide. Moreover, because of the dumbbell shape of the *2p* orbits, the coupling mechanism should be most effective when the metal ions and the oxygen ions

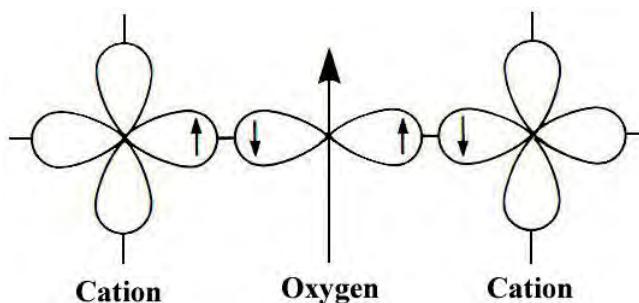lie in one straight line, that is, the angle between the bonds is 180°, and this is the case with

MnO.

Figure 2.8. Schematic representation of the superexchange interaction in the magnetic oxides. The *p* orbital

of an anion (center) interact with the *d* orbitals of the transitional metal cations.

In the case of spinel ferrites the coupling is of the indirect type which involves overlapping of oxygen wave functions with those of the neighboring cations. Consider two transition metal cations separated by an *O*, Fig. 2.8. The O^{2-} has no net magnetic moment since it has completely filled shells, with *p*-type outermost orbitals. Orbital p_x has two electrons: one with spin up, and the other with spin down, consistent with Pauli's exclusion principle. The essential point is that when an oxygen *p* orbital overlaps with a cation *d* orbital, one of the *p* electrons can be accepted by the cations. When one of the transition-metal cations is brought close the O^{2-}, partial electron overlap (between a *3d* electron from the cation and a *2p* electron form the O^{2-}) can occur only for antiparallel spins, because electrons with the same spin are repelled. Empty *3d* states in the cation are available for partial occupation by the O^{2-} electron, with an antiparallel orientation. Electron overlap between the other cation and the O^{2-} then occurs resulting in antiparallel spins and therefore antiparallel order between the cations. Since the *p* orbital are linear,

the strongest interaction is expected to take place for *cation-O^{2-}-cation* angles close to 180^{0} [2].

2.6.2 Néel theory of ferrimagnetism

If we consider the simplest case of a two-sublattice system having antiparallel and non-equal magnetic moments, the inequality may be due to:

1) different elements in different sites,

2) same element in different ionic states, and

3) different crystalline fields leading to different effective moments for ions having the same spin.

The spins on one sublattice are under the influence of exchange forces due to the spins on the second sublattice as well as due to other spins on the same sublattice. The molecular fields acting on the two sublattices A and B can be written as [2, 11-16]

$$\vec{H}_A = \lambda_{AA}\vec{M}_A + \lambda_{AB}\vec{M}_B ,$$

$$\vec{H}_B = \lambda_{AB}\vec{M}_A + \lambda_{BB}\vec{M}_B$$

where $\vec{M}_A$ and $\vec{M}_B$ are the magnetizations of the two sublattices and λ's are the Weiss constants. Since the interaction between the sublattices is antiferromagnetic, λ_{AB} must be negative, but λ_{AA} and λ_{BB} may be negative or positive depending on the crystal structure and the nature of the interacting atoms. Probably, these interactions are also negative, though they are in general quite small.

Assuming all the exchange interactions to be negative the molecular fields will be then given by

$$.\vec{H}_A = -\lambda_{AA}\vec{M}_A - \lambda_{AB}\vec{M}_B ,$$

$$\vec{H}_B = -\lambda_{AB}\vec{M}_A - \lambda_{BB}\vec{M}_B$$

Since in general, λ_{AA} and λ_{BB} are small compared to λ_{AB}, it is convenient to express the strengths of these interactions relative to the dominant λ_{AB} interaction.

Let $\qquad\qquad \lambda_{AA} = \alpha\lambda_{AB}$

and $\qquad\qquad \lambda_{BB} = \beta\lambda_{AB}$

In an external applied field $\vec{H}$, the fields acting on A and B sites are

$$\vec{H}_A = \vec{H} - \lambda_{AB}(\alpha\vec{M}_A - \vec{M}_B),$$

$$\vec{H}_B = \vec{H} - \lambda_{AB}(\vec{M}_A - \beta\vec{M}_B)$$

At temperatures higher than the transition temperature, T_N, $\vec{H}_A$, $\vec{M}_A$ and $\vec{M}_B$ are all parallel and we can write

$$\vec{M}_A = \frac{C_A}{T}[\vec{H} - \lambda_{AB}(\alpha\vec{M}_A - \vec{M}_B)], \qquad\qquad (2.3)$$

$$\vec{M}_B = \frac{C_B}{T}[\vec{H} - \lambda_{AB}(\vec{M}_A - \beta\vec{M}_B)] \qquad\qquad (2.4)$$

where C_A and C_B are the Curie constants for the two sublattices.

$$C_A = N_A g\mu_B^2 S_A(S_A + 1)/3K$$

and $\qquad\qquad C_B = N_B g\mu_B^2 S_B(S_B + 1)/3K$

N_A and N_B denote the number of magnetic ions on A and B sites respectively and S_A and S_B are their spin quantum numbers. Solving for the susceptibility, χ, one gets [2, 11]

$$\frac{1}{\chi} = \frac{T}{C} - \frac{1}{\chi_0} - \frac{b}{T - \theta}$$

$$\frac{1}{\chi} = \frac{T + (C/\chi_0)}{C} - \frac{b}{T - \theta} \qquad (2.5)$$

where C, χ_0, b and θ are constants for particular substance and are given by

$$C = C_A + C_B$$

$$\frac{1}{\chi_0} = -\frac{1}{C^2}[C_A^2 \lambda_{AA} + C_B^2 \lambda_{BB} + 2C_A C_B \lambda_{AB}]$$

$$b = \frac{C_A C_B}{C^3}[C_A^2(\lambda_{AA} - \lambda_{BB})^2 + C_B^2(\lambda_{BB} - \lambda_{AB})^2$$

$$- 2C_A C_B \{\lambda_{AB}^2 - (\lambda_{AA} + \lambda_{BB})\lambda_{AB} + \lambda_{AA}\lambda_{BB}\}]$$

$$\theta = -\frac{C_A C_B}{C}(\lambda_{AB} + \lambda_{BB}) - 2\lambda_{AB}$$

Equation (2.5) represents a hyperbola, and the physically meaning part of it is plotted in Fig. 2.9. This curvature of the plot of $1/\chi$ versus T is a characteristics feature of a ferrimagnet. It cuts the temperature axis at T_C, called the Ferrimagnetic Curie point. At high temperatures the last term of equation (2.5) become negligible, and reduces to a Curie-Weiss law:

$$\chi = \frac{C}{T + (C/\chi_0)}$$

This is the equation of straight line, shown dashed in Fig. 2.9, to which the $1/\chi$ versus T curve becomes asymptotic at high temperatures.
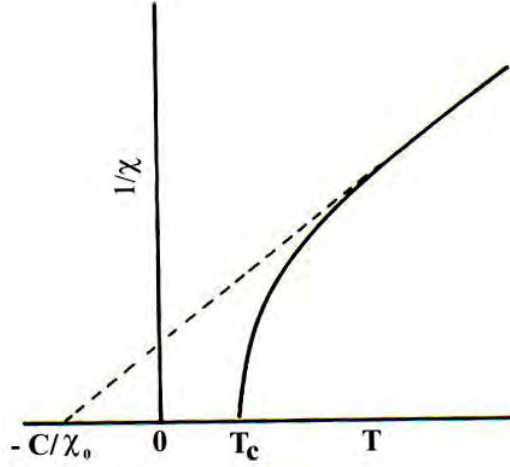
Figure 2.9. The temperature dependence of the inverse susceptibility for ferrimagnets.

The Ferrimagnetic Curie temperature T_C is obtained from equations (2.3) and (2.4) with $H = 0$ and setting the determinant of the coefficients of M_i equal to zero. This gives

$$T_C = \frac{1}{2}[C_A \lambda_{AA} + C_B \lambda_{BB} + \{(C_A \lambda_{AA} - C_B \lambda_{BB})^2 + 4 C_A C_B \lambda_{AB}^2\}^{\frac{1}{2}}] \qquad (2.6)$$

Equation (2.5) is in good agreement with the experiment, except near the Curie point. The experimental Curie temperature, the temperature at which the susceptibility becomes infinite and spontaneous magnetization appears, is lower than the theoretical Curie temperature [11]. This disagreement between theory and experiment in the region of Curie point is presumably due to the short-range spin order (spin clusters) at temperatures above experimental T_C [2, 11].
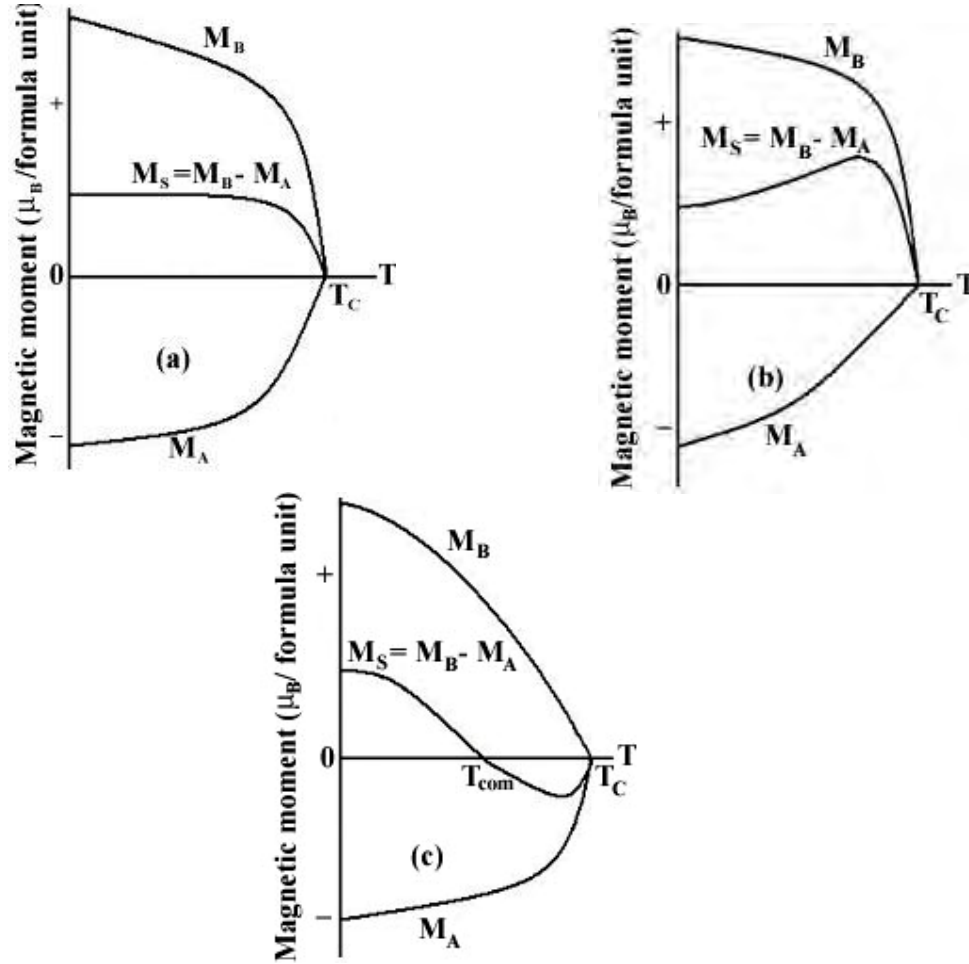
Figure 2.10. Superposition of various combinations of two opposing sublattice magnetizations producing differing resultants including one with a compensation point (schematic).

The sublattice magnetizations will in general have different temperature dependences because the effective molecular fields acting on them are different. This suggests the possibility of having anomaly in the net magnetization versus temperature curves, Fig. 2.10. For most ferrimagnets the curve is similar to that of ferromagnets, but in a few cases there be a compensation point in the curve, Fig. 2.10(c) [1, 11]. At a point below the Curie temperature point, the two sublattice magnetizations are equal and thus appear to have no moment. This

temperature is called the compensation point. Below this temperature one sublattice magnetization is larger and provides the net moment. Above this temperature the other magnetization does dominates and the net magnetization reverses direction.

The essential requisite for Néel configuration is a strong negative exchange interaction between A and B sublattices which results in their being magnetized in opposite directions below the transition point. But there may be cases where intrasublattice interactions are comparable with intersublattice interaction. Néel's theory predicts paramagnetism for such substances at all temperatures. This is unreasonable since strong AA or BB interaction may lead to some kind of ordering especially at low temperature. In the cases of no AB interaction, antiferromagnetic ordering may be expected either in the A or in the B sublattice. Under certain conditions there may be non-collinear spin arrays of still lower energy.

2.6.3 Effect of zinc substitution on the magnetic moments in spinel ferrites

Fe_3O_4 has ferromagnetic properties because of its inverse structure which leads to the formation of domains. A unit cell of Fe_3O_4 contains eight formula units each of which may be written in the form $Fe^{3+}[Fe^{2+}Fe^{3+}]O_4^{2-}$ [13]. Snoek and his co-workers found that oxides of inverse structure could be artificially produced in which the divalent ions of another element, for example Mn, Ni, Co, Mg or Cu, could be substituted for the divalent Fe^{2+} ions in Fe_3O_4. An extensive range of ferrites could thus be made having the general formula $\overrightarrow{Fe}^{3+}[\overleftarrow{M}^{2+}\overleftarrow{Fe}^{3+}]O_4^{2-}$, where arrows indicate spin ordering. Since the

trivalent iron ions are equally distributed on *A* and *B* sites they cancel each other out magnetically, and the magnetic moment per formula unit is then theoretically the same as the magnetic moment of the divalent ion. The *Ni* ferrite has a moment of $2.3\mu_B$ compared with a theoretical value of $2\mu_B$ [1]. *Zn* ferrite is a normal spinel, with $Zn^{2+}(3d^{10})$ ions in *A* sites have zero magnetic moment; Fe^{3+} ions in *B* sites have a magnetic moment $5\mu_B$.

The cation distribution can be written as $Zn^{2+}[\overrightarrow{Fe}^{3+}\overleftarrow{Fe}^{3+}]O_4$, where spin ordering is indicated by arrows. The zero magnetic moment of Zn^{2+} ions leaves trivalent iron ions on *B* sites with a negative *BB* interaction between equal ions. Therefore *Zn* ferrite is not ferromagnetic. Zinc ferrite therefore be expected to be antiferromagnetic and thus to have a Néel point, though measurements show it to be paramagnetic only [1-2, 11, 13].

Magnetic properties can be modified widely by cation substitution. An illustrative case is substitution of *Ni* by *Zn* in *Co* ferrite to form solid solutions $Ni_{1-x}Zn_xFe_2O_4$. The cation distribution can be written as $(Zn_x^{2+}Fe_{1-x}^{3+})[Ni_{1-x}^{2+}Fe_{1+x}^{3+}]O_4^{2-}$ [2]. Zn^{2+} is diamagnetic and its main effect is to break linkages between magnetic cations. Another effect is to increase interaction distance by expanding the unit cell, since it has an ionic radius larger than the *Ni* and *Fe* radii. The most remarkable effect is that substitution of this diamagnetic cation (*Zn*) results in a significant increase in magnetic moment in a number of spinel solid solutions, Fig. 2.11.
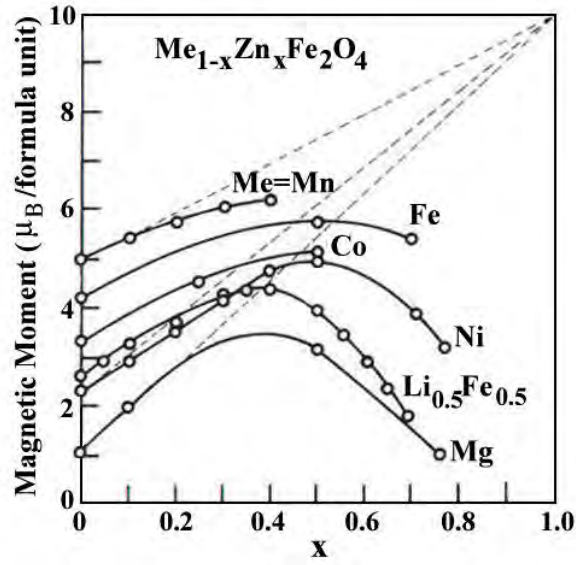
Figure 2.11. Variation of Magnetic moment (in Bohr magnetons per formula unit) with increasing zinc substitution [1, 2].

Magnetic moment as a function of *Zn* content shows an increase for small substitutions, goes through a maximum for intermediate values, decreases and finally vanishes for high *Zn* contents

A simple analysis shows that this increase can be expected for an antiparallel alignment. As the *Zn* content increases, magnetic moments decreases in sublattice *A* and increase in sublattice *B*. If the magnetic moment of *Fe* and *Ni* are 5 and ~2.3 μ_B/ion, respectively, then, per formula unit, the total moment in Bohr magnetons on *B* sublattice is $2.3(1-x) + 5(1+x)$ and on *A* sublattice the total antiparallel moment is $5(1-x)$. If the resultant moment per formula unit is $M_S(0)$, then by taking the difference of *A* and *B* moments [13],

$$M_S(0) = 2.3(1-x) + 5(1+x) - 5(1-x)$$

$$= x(10 - 2.3) + 2.3$$

A linear relationship is obtained with a slope of 7.7, predicting a moment value of $10\mu_B$ per formula unit for *Zn* substitution $x = 1$, as shown by the broken lines in Fig. 2.11. This relationship is not followed over the entire composition range. However, as the *Zn* content increases, $A - O - B$ interactions become too weak and $B - O - B$ interactions begin to dominate. That is, the average distance between the interacting spins gets larger. As a consequence, the system becomes frustrated causing a perturbation to the magnetically ordered spins as large number of *B* sites spins gets non-magnetic impurity atoms as their nearest neighbors.
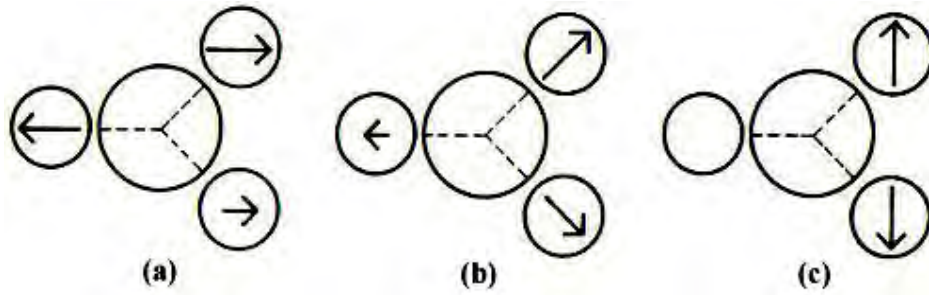
Figure 2.12. Schematic representation of spin arrangements in $Ni_{1-x}Zn_xFe_2O_4$: (a) ferrimagnetic (for $x \leq 0.5$); (b) triangular or Yafet-Kittel (for $x > 0.5$); and (c) antiferromagnetic for $x \approx 1$.

The *B* spins are no longer held in place due to this weak anti-ferromagnetic *A-B* interaction leading to non-collinearity or canting among the *B* sublattice. Thus for $x > 0.5$ *Zn* content, instead of a collinear antiparallel alignment, canted structure appears, where spins in *B* sites are no longer parallel [2, 17], Fig. 2.12. Evidence of this triangular structure has been observed by neutron diffraction [18]; a theoretical analysis showed that departure from collinear order depends on the ratio of the $A - O - B$ to $B - O - B$ molecular field

coefficients, $\lambda_{AB} / \lambda_{BB}$ [19]. For high *Zn* concentration, $B - O - B$ interactions dominant and the ferrite become antiferromagnetic for $x = 1$ [2].

2.7 Microstructure

A polycrystal is much more than many tiny crystals bonded together. The interfaces between the crystals, or the grain boundaries which separate and bond the grains, are complex and interactive interfaces. The whole set of a given material's properties (mechanical, chemical and especially electrical and magnetic) depend strongly on the nature of the microstructure.

In the simplest case, the grain boundary is the region, which accommodates the difference in crystallographic orientation between the neighbouring grains. For certain simple arrangements, the grain boundary is made of an array of dislocations whose number and spacing depends on the angular deviation between the grains. The ionic nature of ferrites leads to dislocation patterns considerably more complex than in metals, since electrostatic energy accounts for a significant fraction of the total boundary energy [2].

For low-loss ferrite, Ghate [1] states that the grain boundaries influence properties by

1) creating a high ressistivity intergranular layer,

2) acting as a sink for impurities which may act as a sintering aid and grain growth modifiers,

3) providing a path for oxygen diffusion, this may modify the oxidation state of cations near the boundaries.

In addition to grain boundaries, ceramic imperfections can impede domain wall motion and thus reduce the magnetic property. Among these are pores, cracks, inclusions, second phases, as well as residual strains. Imperfections also act as energy wells that pin the domain walls and require higher activation energy to detach. Stresses are microstructural imperfections that can result from impurities or processing problems such as too rapid a cool. They affect the domain dynamics and are responsible for a much greater share of the degradation of properties than would expect [1].

Grain growth kinetics depends strongly on the impurity content. A minor dopant can drastically change the nature and concentration of defects in the matrix, affecting grain boundary motion, pore mobility and pore removal [2, 20]. The effect of a given dopant depends on its valence and solubility with respect to host material. If it is not soluble at the sintering temperature, the dopant becomes a second phase which usually segregates to the grain boundary.
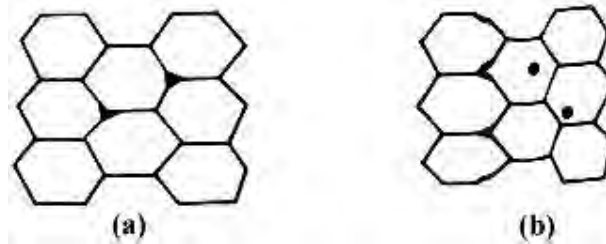
Figure 2.13. Porosity character: (a) intergranular, (b) intragranular.

The porosity of ceramic samples results from two sources, intragranular porosity and intergranular porosity, Fig. 2.13. An undesirable effect in ceramic samples is the formation of exaggerated or discontinuous grain growth which is characterized by the

excessive growth of some grains at the expense of small, neighbouring ones, Fig. 2.14. When this occurs, the large grain has a high defect concentration. Discontinuous growth is believed to result from one or several of the following: powder mixtures with impurities; a very large distribution of initial particle size; sintering at excessively high temperatures; in ferrites containing *Zn* and /or *Mn*, a low O_2 partial pressure in the sintering atmosphere. When a very large grain is surrounded by smaller ones, it is called 'duplex' microstructure.
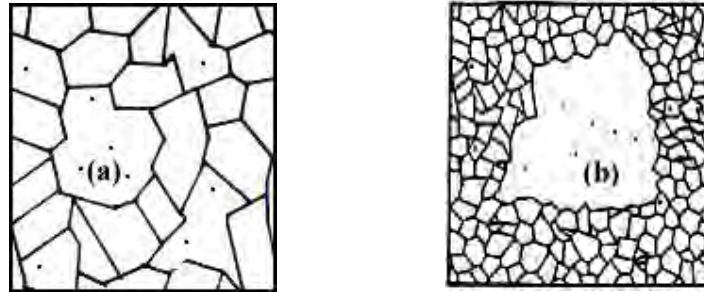
Figure 2.14. Grain growth (a) discontinuous, (b) duplex (schematic).

2.8 Theories of permeability

Permeability is defined as the proportionality constant between the magnetic field induction *B* and applied field intensity *H* [2, 15, and 21]:

$$B = \mu H \tag{2.7}$$

If the applied field is very low, approaching zero, the ratio will be called the initial permeability, Fig. 2.15 and is given by

$$\mu_i = \frac{\Delta B}{\Delta H}_{(\Delta H \to 0)}$$

This simple definition needs further sophistications. A magnetic material subjected to an ac magnetic field can be written as

$$H = H_0 e^{i\omega t} \qquad (2.8)$$

It is observed that the magnetic flux density B lag behind H. This is caused due to the presence of various losses and is thus expressed as

$$B = B_0 e^{i(\omega t - \delta)} \qquad (2.9)$$

Here δ is the phase angle that marks the delay of B with respect to H. The permeability is then given by

$$\mu = \frac{B}{H} = \frac{B_0 e^{i(\omega t - \delta)}}{H_0 e^{i\omega t}} = \frac{B_0 e^{-i\delta}}{H_0} = \frac{B_0}{H_0}\cos\delta - i\frac{B_0}{H_0}\sin\delta = \mu' - i\mu'' \qquad (2.10)$$

where $\qquad \mu' = \frac{B_0}{H_0}\cos\delta \qquad (2.11)$

and $\qquad \mu'' = \frac{B_0}{H_0}\sin\delta \qquad (2.12)$

The real part (μ') of complex permeability (μ), as expressed in equation (2.10) represents the component of B which is in phase with H, so it corresponds to the normal permeability. If there are no losses, we should have $\mu = \mu'$. The imaginary part μ'' corresponds to that of B, which is delayed by phase angle 90^0 from H [11, 15]. The presence of such a component requires a supply of energy to maintain the alternating magnetization, regardless of the origin of delay. The ratio of μ'' to μ', as is evident from equation (2.12) and (2.11) gives

$$\frac{\mu^{//}}{\mu^{/}} = \frac{\dfrac{B_0}{H_0}\sin\delta}{\dfrac{B_0}{H_0}\cos\delta} = \tan\delta \qquad (2.13)$$

This $\tan\delta$ is called loss factor.

The quality factor is defined as the reciprocal of this loss factor, i.e.

$$\text{Quality factor} = \frac{1}{\tan\delta} \qquad (2.14)$$

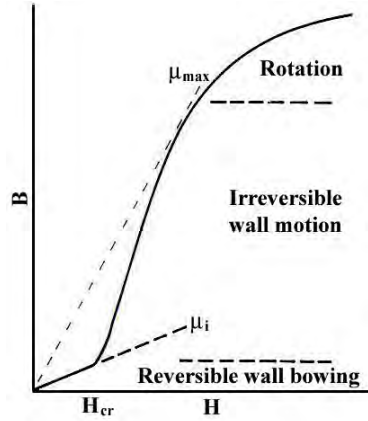And the relative quality factor, $Q = \dfrac{\mu^{/}}{\tan\delta}$ $\qquad (2.15)$

Figure 2.15. Schematic magnetization curve showing the important parameter: initial permeability, μ_i (the

slope of the curve at low fields) and the main magnetization mechanism in each magnetization range.

The curves that show the variation of both $\mu^{/}$ and $\mu^{//}$ with frequency are called

the magnetic spectrum or permeability spectrum of the material [19]. The variation of

permeability with frequency is referred to as dispersion. The measurement of complex

permeability gives us valuable information about the nature of domain wall and their

movements. In dynamic measurements the eddy current loss is very important. This

occurs due to the irreversible domain wall movements. The permeability of a ferrimagnetic substance is the combined effect of the wall permeability and rotational permeability mechanisms.

2.8.1 Mechanisms of permeability

The mechanisms can be explained as follows: A demagnetized magnetic material is divided into number of Weiss domains separated by Bloch walls. In each domain all the magnetic moments are oriented in parallel and the magnetization has its saturation value M_s. In the walls the magnetization direction changes gradually from the direction of magnetization in one domain to that in the next. The equilibrium positions of the walls result from the interactions with the magnetization in neighboring domains and from the influence of pores; crystal boundaries and chemical inhomogeneities which tend to favour certain wall positions.

2.8.1.1 Wall permeability

The mechanism of wall permeability arises from the displacement of the domain walls in small fields. Lets us consider a piece of material in the demagnetized state, divided into Weiss domains with equal thickness L by means of 180° Bloch walls (as in the Fig. 2.16). The walls are parallel to the YZ plane. The magnetization M_s in the domains is oriented alternately in the $+Z$ or $-Z$ direction. When a field H with a component in the $+Z$ direction is applied, the magnetization in this direction will be favoured. A displacement dx of the walls in the direction shown by the dotted lines will decrease the energy density by an amount [22, 23]:

$$\frac{2M_s H_z dx}{L}$$

This can be described as a pressure $M_s H_z$ exerted on each wall. The pressure will be counteracted by restoring forces which for small deviations may assume to be kdx per unit wall surface. The new equilibrium position is then given by

$$d = \frac{M_s H_z dx}{L}$$

From the change in the magnetization

$$\Delta M = \frac{2M_s d}{L},$$

the wall susceptibility χ_w may be calculated. Let H makes the angle θ with Z direction. The magnetization in the θ direction becomes

$$(\Delta M)_\theta = \frac{2M_s d}{L}\cos\theta \text{ , And with } H_z = H\cos\theta \text{ and } d = \frac{2M_s H_z}{K}$$

we obtain

$$\chi_w = \frac{(\Delta M)_\theta}{H} = \frac{4M_s^2 \cos^2\theta}{KL} \tag{2.16}$$
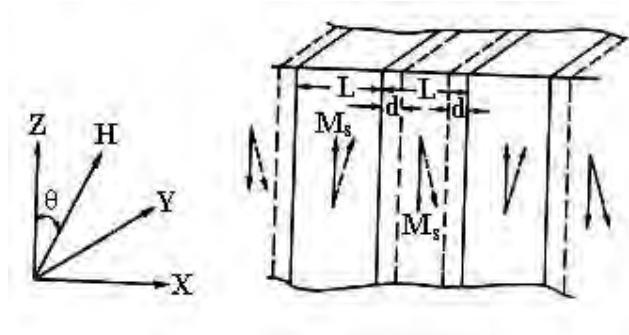
Figure 2.16. Magnetization by wall motion and spin rotation.

2.8.1.2 Rotational permeability

The rotational permeability mechanism arises from rotation of the magnetization in each domain. The direction of M can be found by minimizing the magnetic energy E as a function of the orientation. Major contribution to E comes from the crystal anisotropy energy. Other contributions may be due to the stress and shape anisotropy. The stress may influence the magnetic energy via the magnetostriction. The shape anisotropy is caused by the boundaries of the sample as well as by pores, nonmagnetic inclusions and inhomogeneities. For small angular deviations, α_x and α_y may be written as

$$\alpha_x = \frac{M_x}{M_s} \text{ and } \alpha_y = \frac{M_y}{M_s}.$$

For equilibrium Z-direction E may be expressed as [16, 17]

$$E = E_0 + \frac{1}{2}\alpha_x^2 E_{xx} + \frac{1}{2}\alpha_y^2 E_{yy}$$

where it is assumed that x and y are the principal axes of the energy minimum. Instead of E_{xx} & E_{yy}, the anisotropy field H_x^A and H_y^A are often introduced. Their magnitude is given by

$$H_x^A = \frac{E_{xx}}{2M_s} \text{ and } H_y^A = \frac{E_{yy}}{2M_s},$$

H_x^A & H_y^A represent the stiffness with which the magnetization is bound to the equilibrium direction for deviations in x and y direction, respectively. The rotational susceptibilities $\chi_{r,x}$ and $\chi_{r,y}$ for fields applied along x and y directions, respectively are

$$\chi_{r,x} = \frac{M_s}{H_x^A} \text{ and } \chi_{r,y} = \frac{M_s}{H_y^A}.$$

For cubic materials it is often found that H_x^A and H_y^A is equal. For $H_x^A = H_y^A = H^A$ and a field H which makes an angle θ with the Z direction (as shown in Fig. 2.16) the rotational susceptibility, $\chi_{r,c}$ in one crystallite becomes

$$\chi_{r,c} = \frac{M_s}{H^A} \sin^2 \theta \qquad\qquad (2.17)$$

A polycrystalline material consisting of a large number of randomly oriented grains of different shapes, with each grain divided into domains in a certain way. The rotational susceptibility χ_r of the material has to be obtained as a weighted average of $\chi_{r,c}$ of each crystallite, where the mutual influence of neighbouring crystallites has to be taken into account. If the crystal anisotropy dominates other anisotropies, then H^A will be constant throughout the material, so only the factor $\sin^2 \theta$ (equation 2.17) has to be averaged. Snoek [24] assuming a linear averaging of $\chi_{r,c}$ and found

$$\chi_r = \frac{2M_s}{3H^A}$$

The total internal susceptibility

$$\chi = \chi_w + \chi_r = \frac{4M_s^2 \cos^2 \theta}{KL} + \frac{2M_s}{3H^A} \qquad\qquad (2.18)$$

If the shape and stress anisotropies cannot be neglected, H^A will be larger. Any estimate of χ_r will then be rather uncertain as long as the domain structure, and the pore distribution in the material are not known. A similar estimate of χ_w would require knowledge of the stiffness parameter k and the domain width L. These parameters are

influenced by such factors as imperfection, porosity and crystallite shape and distribution which are essentially unknown.

References

[1]   Goldman, A. *Handbook of Modern Ferromagnetic Materials*, Kulwer Acad. Pub, Boston, U.S.A (1999).

[2]   Valenzuela, R. *Magnetic Ceramics*, Cambridge University Press, Cambridge (1994).

[3]   Caltun Ovidiu F., Leonard Spinu, "Magnetic properties of high frequency NiZn ferrites doped with CuO," *IEEE Trans. Magn.,* **37(4),** 1 (2001).

[4]   Chul Sung Kim, Woo Chul Kim, Sung Yong An, Seung Wha Lee, "Structure and mossbauer studies of Cu-dopped NiZn ferrites," *J. Magn. Magn. Mater*., **213**, 215-216 (2000).

[5]   Rahman, I.Z. and Ahmed, T. T., "A study on Cu substituted chemically processed Ni-Zn-Cu ferrites", *J. Magn. Magn. Mater*., 290-291, 1576-1579 (2005).

[6]   Kim, Woo Chul, Sa Jin Kim,, Seung Wha Lee, Chul Sung Kim, "Growth of ultrafine NiCuZn ferrite and magnetic properties ," *J. Magn. Magn. Mater*., **226 230(2)**,1418 (2001).

[7]   Nakamura, T., "Low temperature sintering of Ni-Zn-Cu ferrire and its permeability spectra," *J. Magn. Magn. Mater*., **168**, 285.(1997).

[8]   Rosales, M. I., Plata, A. M., Nicho, M. E., Brito, A., Ponce, M. A., Castano, V. M., "Effect of sintering conditions on microstructure and magnetic properties on Mn-Zn ferrites," J. Mater. Sci., **30** (1995) 4446-4450.

[9]   Chien, Y., Ko, Y., "Dependence of magnetic properties of Mn-Zn ferrites on the degree of calcination," J. J. Mater. Sci., **26** (1991) 5859-5864.

[10]   Globus, A., *2nd EFS Conf. on Soft Magnetic Materials*, Wolfson Center for Magnetic Technology, Cardiff, Wales (1975).

[11]   Cullity, B. D., *Introduction to Magnetic Materials*, Addison-Wisley Publishing Company, Inc., California (1972).

[12]   Wahab, M. A., *Solid State Physics: Structure and Properties of Materials*, Narosa Publishing House, New Delhi (1999).

[13]   Brailsford, F., *Physical Principles of Magnetism*, D. Van Nostrand Company Ltd., London (1966).

[14]   Dekker, A. J., *Solid State Physics*, Macmillan India Ltd., New Delhi (1998).

[15]   Chikazumi, S., *Physics of Magnetism*, Jhon Wiley & Sons, Inc., New York (1966).

[16]   Kittel, C., *Introduction to Solid State Physics*, 7th edition, Jhon Wiley & Sons, Inc., Singapore (1996).

[17]   Hossain, A. K. M. A., Seki, M., Kawai, T. and Tabata, H., "Colossal magnetoresistance in spinel type $Zn_{1-x}Ni_xFe_2O_4$," *J. Appl. Phys.*, **96**, 1273 (2004).

[18]   Murthy, N. S. S., Natera, M. G. and Youssef, S. I., "Yafet-Kittel angles in nickel-zinc ferrites," *Physical Review*, **181**, 969 (1969).

[19]   Yafet, Y. and Kittel, C., "Antiferromagnetic arrangements in ferrites," *Physical Review*, **87**, 290 (1952).

[20]   Yan, M. F. and Johnson, D. W., "Impurity induced exaggerated grain growth in Mn-Zn ferrites," *J. Am. Ceram. Soc.*, **61**, 342 (1978).

[21]   Hadfield, D., *Permanent Magnets and Magnetism*, Jhon Wiley & Sons, Inc., New York (1962).

[22]   Sikder, S. S., "Temperature dependence of magnetization and induced magnetic anisotropy of some Fe, Co and Ni-based amorphous ribbons," *Ph. D. Thesis*, BUET, Bangladesh (1999).

[23]   Hussain, K. M. A., "Study of complex permeability and secondary effects in some cobalt and manganese based ferrites," *M. Phil. Thesis*, BUET, Bangladesh (2003).

[24]   Snoek, J. L., "Dispersion and absorptions in magnetic ferrites at frequencies above Mc/s," *Physica*, **14**, 207 (1948).

CHAPTER 3

SAMPLE PREPARATION

Scientists around the world are preparing various ferrites using different techniques. Properties and characteristics of ferrites depend very much on preparation technique. In this chapter we describe how the ferrites samples are prepared for investigations of various properties.

3.1 Introduction

A goal common to all the ferrites is the formation of the spinel structure. Now a days, the majority of ferrite powders are made by the conventional Ceramic process or Solid State Reaction technique. Most of the non-conventional processes are involved in producing the powder by a wet method. Among these methods, some are [1, 2]:

1) Co-precipitation

2) Organic precursors

3) Sol-gel synthesis

4) Spray-drying

5) Freeze-drying

6) Combustion synthesis

7) Glass crystallization

In this chapter, we describe the solid state reaction method that is used in this research work.

3.2 Conventional solid state reaction method

In the solid state reaction method, the required composition is usually prepared from the appropriate amount of raw mineral oxides or carbonates by crushing, grinding and milling. The most common type of mill is the ball mill, which consists of a lined pot with hard spheres or rod inside. Milling can be carried out in a wet medium to increase the degree of mixing. This method depends on the solid state inter-diffusion between the raw materials. Solids do not usually react at room temperature over normal time scales. Thus it is necessary to heat them at higher temperatures for the diffusion length $(2\Delta t)^{1/2}$ to exceed the particle size, where Δ is the diffusion constant for the fast-diffusing species, and t is the firing time. The ground powders are then calcined in air or oxygen at a temperature above 1000°C. For some time, this process is continued until the mixture is converted into the correct crystalline phase. The calcined powders are again crushed into fine powders. The pellets or toroid shaped samples are prepared from these calcined powders using die-punch assembly or hydrostatic or isostatic pressure. Sintering is carried out in the solid state, at temperature ranging 1100-1400°C, for times of typically 1-40 h and in various atmospheres (e.g. Air, O_2 and N_2) [3-6]. Fig. 3.1 shows, diagrammatically, the stages followed in ferrite preparation.

The general solid state reaction leading to a ferrite *MeFe$_2$O$_4$* may be represented as

$$MeO + Fe_2O_3 \longrightarrow MeFe_2O_4$$
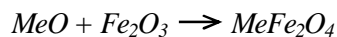
where *Me* is the divalent ions. There are basically four steps in the preparation of ferrite:

1) Preparation of materials to form an intimate mixture with the metal ions in the ratio which they will have in the final product,

2) Heating of this mixture to form the ferrite (often called calcining),

3) Grinding the calcined powders and pressing the fine powders into the required shape, and

4) Sintering to produce a highly densified product.

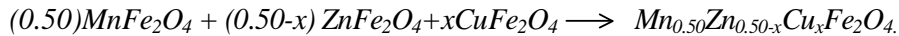## 3.3 Details of calcining, pressing and sintering

Calcining is defined as the process of obtaining a homogeneous and phase pure composition of mixed powders by heating them for a certain time at a high temperature and then allowing it to cool slowly. During the calcining stage, the reaction of Fe_2O_3 with metal oxide (say, MeO or Me'_2O_3) takes place in the solid state to form spinel according to the reactions [7]:

$$MeO + Fe_2O_2 \longrightarrow MeFe_2O_4 \text{ (Spinel)}$$

$$2Me'_2O_3 + 4Fe_2O_3 \longrightarrow 4Me'Fe_2O_4 \text{ (Spinel)} + O_2$$
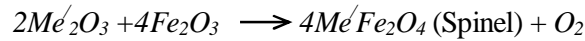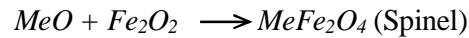
The $MnCO_3$, ZnO and Cu_2O creeps into Fe_2O_3 as below, to form an intermediate phase

$$Fe_2O_3 + MnCO_3 \longrightarrow MnFe_2O_4 + CO_2$$

$$Fe_2O_3 + ZnO \longrightarrow ZnFe_2O_4$$

$$4Fe_2O_3 + 2Cu_2O + O_2 \longrightarrow 4CuFe_2O_4$$

And lastly

$$(0.50)MnFe_2O_4 + (0.50-x)\,ZnFe_2O_4 + xCuFe_2O_4 \longrightarrow Mn_{0.50}Zn_{0.50-x}Cu_xFe_2O_4.$$

```
┌─────────────────────────────┐
│    Oxides of raw materials   │
└─────────────────────────────┘
              ↓
┌─────────────────────────────┐
│     Weighing by different    │
│        mole percentage       │
└─────────────────────────────┘
              ↓
┌─────────────────────────────┐
│      Dry mixing by agate     │
│            mortar            │
└─────────────────────────────┘
              ↓
┌─────────────────────────────┐
│      Wet mixing by ball      │
│            milling           │
└─────────────────────────────┘
              ↓
┌─────────────────────────────┐
│            Drying            │
└─────────────────────────────┘
              ↓
┌─────────────────────────────┐
│           Calcining          │
└─────────────────────────────┘
              ↓
┌─────────────────────────────┐
│      Milling and adding      │
│            binder            │
└─────────────────────────────┘
              ↓
┌─────────────────────────────┐
│     Pressing to desired      │
│            shapes            │
└─────────────────────────────┘
              ↓
┌─────────────────────────────┐
│           Sintering          │
└─────────────────────────────┘
              ↓
┌─────────────────────────────┐
│      Finished products       │
└─────────────────────────────┘
```
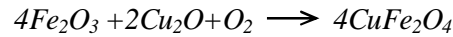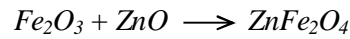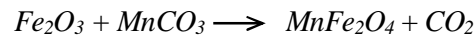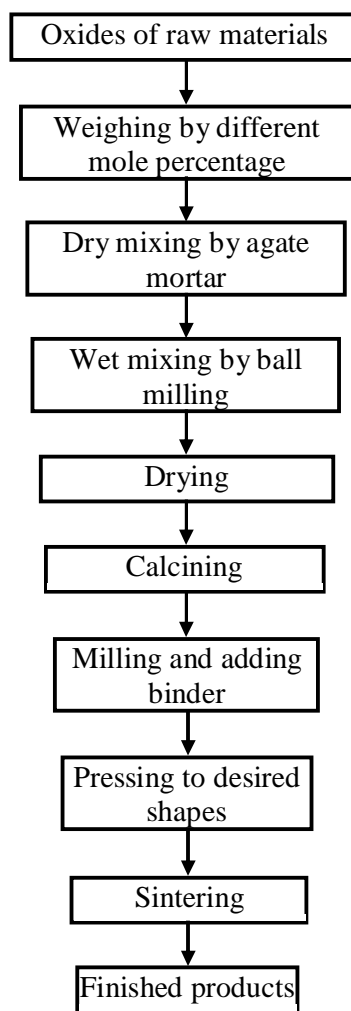
Figure 3.1. Flow chart of the stages in preparation of spinel ferrite.

The calcining process can be repeated several times to obtain a high degree of homogeneity. The calcined powders are crushed into fine powders. The ideal characteristics of fine powders are [2]:

1) small particle size (sub micron)

2) narrow distribution in particle size

3) dispersed particles

43

4) equiaxed shape of particles

5) high purity

6) homogeneous composition.

A small particle size of the reactant powders provides a high contact surface area for initiation of the solid state reaction; diffusion paths are shorted, leading to more efficient completion of the reaction. Porosity is easily eliminated if the initial pores are very small. A narrow size distribution of spherical particles as well as a dispersed state is important for compaction of the powder during green-body formation. Grain growth during sintering can be better controlled if the initial size is small and uniform.

A binder is usually added prior to compaction, at a concentration lower than 5wt % [2]. Binders are polymers or waxes; the most commonly used binder in ferrite is polyvinyl alcohol. The binder facilitates the particles flow during compacting and increases the bonding between the particles, presumably by forming bonds of the type *particle-binder-particle*. During sintering, binders decompose and are eliminated from the ferrite. Pressures are used for compacting very widely but are commonly several tons per square inch (i. e., up to $10^8 \, N \, m^{-2}$).

Sintering is defined as the process of obtaining a dense, tough body by heating a compacted powder for a certain time at a temperature high enough to significantly promote diffusion, but clearly lower than the melting point of the main component. The driving force for sintering is the reduction in surface free energy of the powder. Part of this energy is transferred into interfacial energy (grain boundaries) in the resulting polycrystalline body [2, 8]. The sintering time, temperature and the furnace atmosphere play very important role on the magnetic property of ferrite materials.

The purposes of sintering process are:

1) to bind the particles together so as to impart sufficient strength to the product,

2) to densify the material by eliminating the pores and

3) to homogenize the materials by completing the reactions left unfinished in the

    calcining step.

Sintering of crystalline solids is dealt by Coble and Burke [9] who found the

following empirical relationship regarding rate of grain growth:

$$\bar{d} = kt^n$$

where $\bar{d}$ is the mean grain size, n is about 1/3, t is sintering time and k is a temperature

dependent parameter. Sintering is divided into three stages, Fig. 3.2 [2, 10].

Stage 1. Contact area between particles increases,

Stage 2. Porosity changes from open to closed porosity,

Stage 3. Pore volume decreases; grains grow.
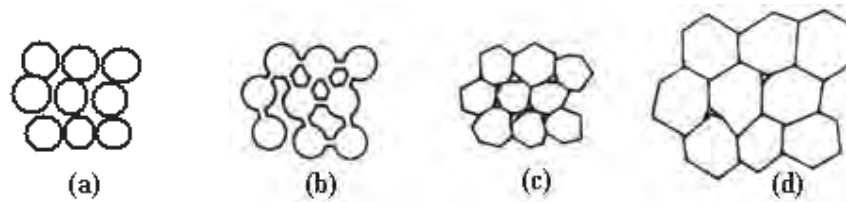
Figure 3.2. Schematic representation of sintering stages: (a) greenbody, (b) initial stage, (c) intermediate stage, and (d) final stage.

In the initial stage, neighbouring particles form a neck by surface diffusion and

presumably also at high temperatures by an evaporation-condensation mechanism. Grain

growth begins during the intermediate stage of sintering. Since grain boundaries are the sinks for vacancies, grain growth tends to decrease the pore elimination rate due to the increase in distance between pores and grain boundaries, and by decreasing the total grain boundary surface area. In the final stage, the grain growth is considerably enhanced and the remaining pores may become isolated.

In *Mn-Zn* ferrites, the presence of *Zn* complicates the sintering process because high temperature coupled with low oxygen firing will cause *Zn* loss. High density is important for high permeability, but so is *Zn* conservation. Tasaki [1] described two alternative firings to achieve high density:

1) Low sintering temperature excluding O_2 (Vacuum, argon, nitrogen),

2) High temperature in pure oxygen to reduce *Zn* loss.

Accordingly, other properties correlated along with density:

1) Lattice constant is greater for O_2, smaller for vacuum

2) Curie temperature is greater for vacuum, smaller for O_2

3) Resistivity is greater for O_2, smaller for vacuum.

3.4 Preparation of the present samples

Various $Mn_{0.50}Zn_{0.50-x}Cu_xFe_2O_4$ (with x=0.00, 0.02, 0.05, 0.08, 0.10, 0.15, 0.20, 0.25, 0.30) compositions were prepared by the standard solid-state reaction technique. High purity powders of $MnCO_3$ (99.99%), ZnO (99.99%), Cu_2O (99.99%), Fe_2O_3 (99.8%) were used as raw materials. Approximate amount of required powders were weighted and mixed thoroughly and then calcined at 950°C for 5 h. The calcined powders were then pressed into disk- and toroid-shaped samples. The samples were sintered at

various temperatures (1200, 1250 and 1300°C) in air for 5 h. The temperature rate was 10

^{o}C/ min for heating and 5 ^{o}C/ min for cooling.

Figure 3.3 Toroid shaped Samples.

References

[1]   Goldman, A. *Handbook of Modern Ferromagnetic Materials*, Kulwer Acad. Pub, Boston, U.S.A
        1999

[2]   Valenzuela, R. *Magnetic Ceramics*, Cambridge University Press, Cambridge , 1994

[3]   Hossain, A. K. M. A, "Investigation of colossal magnetoresistance in bulk and thick film
        magnetites," *Ph. D. Thesis*, Imperial College, London , 1998.

[4]   Cullity, B. D. *Introduction to Magnetic Materials*, Addison-Wisley Publishing Company, Inc.,
        California , 1972

[5]   Brook, R. J. *Sintering: An Overview, Concise Encyclopedia of Advanced Ceramic Materials*,
        Pergamon Press, Oxford, pp. 438 ,1991.

[6]   Reijnen, P. *Science of Ceramics*, Academic Press, London , 1967

[7]   Slick, P. I. *Ferrites for Non-microwave Applications*, Vol. 2, North Holland Pub. Co. ,1980.

[8]   Kingery, W. D, Bowen , H. K. and Uhlman , D. R., *Introduction to Ceramics*, 2nd edition, Wiley
        Interscience, Newyork, pp. 476 , 1976

[9]   Coble , R. L. and Burke, J. E. *4th Int. Symp. On the Reactivity of Solids*, Amsterdam, pp. 38-51
        1960.

[10]   McColm, I. J and Clark , N. J. *Forming, Shaping and Working of high Performance Ceramics*,
        Blackie, Glasgow, pp. 1-338 , 1988.

CHAPTER 4

EXPERIMENTAL TECHNIQUES

In this chapter we describe basic experimental techniques to measure the lattice parameters and frequency dependent AC permeability of ferrite samples. We describe also the experimental technique for the measurement of temperature dependent initial permeability. The Néel temperatures of the samples were determined from this temperature dependent initial permeability.

4.1 X-ray diffraction

Bragg reflection is a coherent elastic scattering in which the energy of the X-ray is not changed on reflection. If a beam of monochromatic radiation of wavelength λ is incident on a periodic crystal plane at an angle θ and is diffracted at the same angle as shown in Fig. 4.1, the Bragg diffraction condition for X-rays is given by

$$2d\, Sin\theta = n\lambda \tag{4.1}$$

where *d* is the distance between crystal planes and *n* is the positive integer which represents the order of reflection. Equation (4.1) is known as Bragg law. This Bragg law suggests that the diffraction is only possible when $\lambda \leq 2d$ [1]. For this reason we cannot use the visible light to determine the crystal structure of a material. The X-ray diffraction (XRD) provides substantial information on the crystal structure.
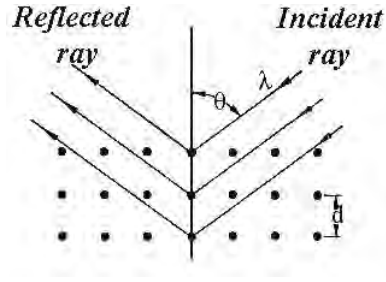
Figure 4.1. Bragg law of diffraction.

X-ray diffraction was carried out with an X-ray diffractometer for various $Mn_{0.50}Zn_{0.50-x}Cu_xFe_2O_4$ (x = 0.00, 0.02, 0.05, 0.08, 0.10, 0.15, 0.20, 0.25, 0.30). For this purpose monochromatic Cu-K_α radiation was used. The lattice parameter for each peak of each sample was calculated by using the formula

$$a = d\sqrt{h^2 + k^2 + l^2} \tag{4.2}$$

where h, k and l are the indices of the crystal planes. To determine the exact lattice parameter for each sample, Nelson-Riley method was used. The Nelson-Riley function $F(\theta)$ is given as

$$F(\theta) = \frac{1}{2}\left[\left(Cos^2\theta / Sin\theta\right) + \left(Cos^2\theta / \theta\right)\right] \tag{4.3}$$

The values of lattice constant 'a' of all the peaks for a sample are plotted against $F(\theta)$. Then using a least square fit method exact lattice parameter 'a_o' is determined. The point where the least square fit straight line cut the y-axis (i.e. at $F(\theta) = 0$) is the actual lattice parameter of the sample. The theoretical density ρ_{th} was calculated using following expression:

$$\rho_{th} = \frac{8M}{N_A\, a_o^3}\, g/cm^3 \tag{4.4}$$

49

where N_A is Avogadro's number (6.023×10^{23} mol^{-1}), M is the molecular weight. The porosity was calculated from the relation $\{100(\rho_{th} - \rho_B)/\rho_{th}\}\%$, where ρ_B is the bulk density measured by the formula $\rho_B = M/V$ [2].

4.2 Study of microstructure

The microstructural study was performed in order to have an insight of the grain structures. The samples of different compositions and sintered at different temperatures were chosen for this purpose. The samples were visualized under a high-resolution optical microscope (Olympus DP 70) and then photographed. Average grain sizes (grain diameter) of the samples were determined from optical micrographs by linear intercept technique [3]. To do this, several random horizontal and vertical lines were drawn on the micrographs. Therefore, we counted the number of grains intersected and measured the length of the grains along the line traversed. Finally the average grain size was calculated.

4.3 Complex permeability measurement

For high frequency application, the desirable property of a ferrite is high permeability with low loss. One of the most important goals of ferrite research is to fulfill this requirement. The techniques of permeability measurement and frequency characteristics of the present samples are described in sections 4.3.1 and 4.3.2.

4.3.1 Techniques for the permeability measurement

Measurements of permeability normally involve the measurements of the change in self-inductance of a coil in presence of the magnetic core. The behaviour of a self-inductance can now be described as follows. We assume an ideal loss less air coil of inductance L_0. On insertion of a magnetic core with permeability μ, the inductance will be μL_0. The complex impedance Z of this coil [4] can be expressed as follows:

$$Z = R + jX = j\omega L_0 \mu = j\omega L_0(\mu' - j\mu'') \tag{4.5}$$

where the resistive part is $\qquad\qquad R = \omega L_0 \mu'' \qquad\qquad\qquad\qquad$ (4.6)

and the reactive part is $\qquad\qquad X = \omega L_0 \mu' \qquad\qquad\qquad\qquad$ (4.7)

The RF permeability can be derived from the complex impedance of a coil, Z, given by equation (4.5). The core is taken as toroidal to avoid demagnetizing effects. The quantity L_o is derived geometrically as shown in section 4.3.2.

4.3.2 Frequency characteristics of the present samples

The frequency characteristics of the ferrite samples i.e. the initial permeability spectra were investigated using a Wayne Kerr Precision Impedance Analyzer (model no. 6500B) and Agilent Precision Impedance Analyzer (model no. 4294A). The complex permeability measurements on toroid shaped specimens were carried out at room temperature on all the samples in the frequency range 1 kHz - 120 MHz. The real part (μ_i') and imaginary part (μ_i'') of the complex permeability were calculated using the following relations [4]: $\mu_i' = L_s/L_0$ and $\mu_i'' = \mu_i' \tan\delta$, where L_s is the self-inductance of the sample core and $L_0 = \mu_o N^2 S/\pi\overline{d}$ is derived geometrically. Here L_o is the inductance

of the winding coil without the sample core, N is the number of turns of the coil ($N = 4$), S is the area of cross section of the toroidal sample as given below:

$$S = d \times h,$$

where

$$d = \frac{d_2 - d_1}{2},$$

$$d_1 = \text{Inner diameter},$$

$$d_2 = \text{Outer diameter},$$

$$h = \text{Height}$$

and $\bar{d}$ is the mean diameter of the toroidal sample as given below:

$$\bar{d} = \frac{d_1 + d_2}{2}$$

The relative quality factor is determined from the ratio $\dfrac{\mu_i^{/}}{\tan \delta}$.

4.4 Néel temperature measurement

Néel temperature measurement is one of the most important measurements for magnetic materials. Néel temperature provides substantial information on magnetic status of a substance in respect of the strength of exchange interaction. So, the determination of Néel temperature is of great importance.

Néel temperature was measured from the temperature dependent initial permeability. For this measurement, the sample was kept inside a cylindrical oven with a thermocouple placed at the middle of the sample. The thermocouple measures the temperature inside the oven and also of the sample. The sample was kept just in the middle part of the cylindrical oven in order to minimize the temperature gradient. The

temperature of the oven was then raised slowly. If the heating rate is very fast then temperature of the sample may not follow the temperature inside the oven, and there can be misleading information on the temperature of sample. The thermocouple showing the temperature in that case will be erroneous. Therefore, a slow heating rate was used to eliminate this problem. Also, a slow heating ensures accuracy in the determination of Néel temperature. The oven was kept thermally insulated from the surroundings. The temperature dependent permeability was measured at a constant frequency (100 kHz) of a sinusoidal wave.

4.5 DC magnetization measurement

The magnetization (M) measurements were made on pieces of the samples (approximate dimensions $2 \times 1 \times 1 \text{ mm}^3$) using the Superconducting Quantum Interface Device (SQUID) magnetometer (MPMS-5S; Quantum design Co. Ltd.).

References

[1]   Kittel, C., *Introduction to Solid State Physics*, 7th edition, Jhon Wiley & Sons, Inc., Singapore, 1996.

[2]   Cullity, B. D., *Introduction to Magnetic Materials*, Addison-Wesley Publishing Company, Inc., California, 1972.

[3]   Hossain, A. K. M. A, "Investigation of colossal magnetoresistance in bulk and thick film magnetites," *Ph. D. Thesis*, Imperial College, London, 1998.

[4]   Goldman, A., *Handbook of Modern Ferromagnetic Materials*, Kulwer Acad. Pub, Boston, U.S.A, 1999.

CHAPTER 5

RESULTS AND DISCUSSION

The polycrystalline $Mn_{0.50}Zn_{0.50-x}Cu_xFe_2O_4$ (x = 0.00, 0.02, 0.05, 0.08, 0.10, 0.15, 0.20, 0.25, 0.30) are studied. All ferrites are sintered at various temperatures (1200, 1250, and 1300°C) for five hours in air. Structural and surface morphology are studied by X-ray diffraction and optical microscopy. The magnetic properties of the ferrites are characterized with high frequency (1 kHz-120 MHz) complex permeability and temperature dependent permeability measurements. DC Magnetizations of all samples are also studied. The effects of Cu substitution and sintering temperature on the complex permeability of these ferrites are discussed.

5. Investigation of polycrystalline $Mn_{0.50}Zn_{0.50-x}Cu_xFe_2O_4$ ferrites

5.1 Lattice parameters, density and porosity

The X-ray diffraction (XRD) patterns for various $Mn_{0.50}Zn_{0.50-x}Cu_xFe_2O_4$ (x = 0.00, 0.02, 0.05, 0.08, 0.10, 0.15, 0.20, 0.25, 0.30) are shown in Fig. 5.1. The patterns clearly show their single phase and formation of spinel structure. Analyzing the XRD patterns it was observed that the positions of the peaks comply with the reported value [1]. The lattice parameter, density, porosity and average grain size for different samples sintered at different temperatures are given in Table 5.1. It is noticed from Fig. 5.2 that the lattice constant decreases with increasing of Cu^{2+} doping in the $Mn_{0.50}Zn_{0.50-x}Cu_xFe_2O_4.$ The decrease in lattice constant with increasing Cu^{2+} substitution can be explained in terms of ionic radii. The radius of Zn^{2+} (0.74 Å) is greater than that of Cu^{2+} (0.65 Å) [2]. Fig. 5.2 shows the variation of lattice parameter with F(θ) and the variation of lattice constant with x for various $Mn_{0.50}Zn_{0.50-x}Cu_xFe_2O_4.$
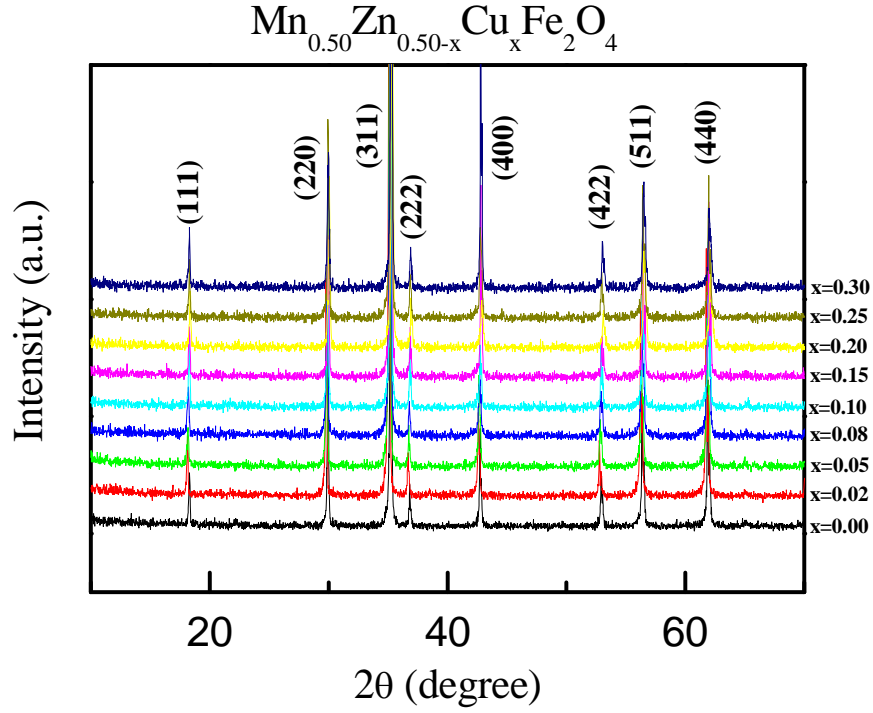
Fig. 5.1. The X-ray diffraction patterns for $Mn_{0.50}Zn_{0.50-x}Cu_xFe_2O_4$.
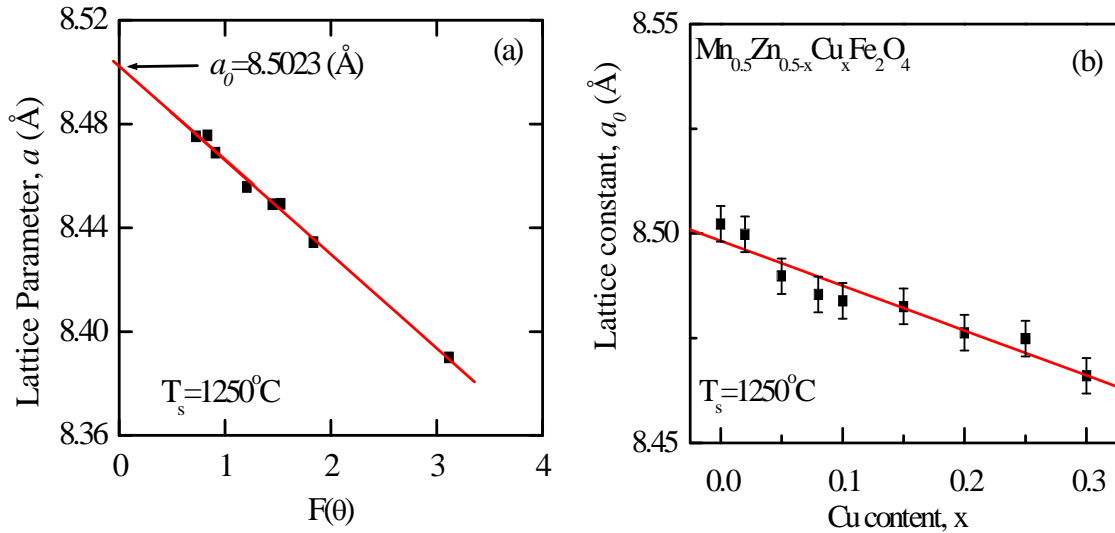
Fig. 5.2. (a) The variation of lattice parameter 'a' with F(θ) and (b) the variation of lattice constant a_o with

x for $Mn_{0.50}Zn_{0.50-x}Cu_xFe_2O_4$

Table 5.1. The lattice constant, sintering temperature, density, porosity, and average grain size of the

$Mn_{0.50}Zn_{0.50-x}Cu_xFe_2O_4$ samples sintered at various temperatures with fixed dwell time 5 h.

x	a_o (Å)	T_s (°C)	P_{th} (g/cm³)	ρ_B (g/cm³)	P (%)	T_N (°C)	Grain size (μm)	$\mu_i^{/}$ (at 100 kHz)
0.00	8.5023	1200	5.0970	4.29	15.85	-	15.50	469
		1250		4.31	15.51		-	657
		1300		4.28	15.99		-	283
0.02	8.4998	1200	5.1008	4.38	14.17	-	17.05	485
		1250		4.59	10.09		-	742
		1300		4.36	14.59		-	302
0.05	8.4898	1200	5.1177	4.40	13.95	80	18.41	589
		1250		4.75	7.24		-	800
		1300		4.37	14.61		-	303
0.08	8.4854	1200	5.1244	4.45	13.27	-	22.03	645
		1250		4.79	6.62		-	822
		1300		4.40	14.08		-	334
0.10	8.4839	1200	5.1263	4.46	13.01	119	25.36	675
		1250		4.82	5.90		-	849
		1300		4.54	11.51		-	351
0.15	8.4826	1200	5.1267	4.42	13.86	186	26.52	489
		1250		4.81	6.27		-	816
		1300		4.40	14.24		-	322
0.20	8.4763	1200	5.1361	4.28	16.66	200	26.79	400
		1250		4.75	7.55		-	746
		1300		4.29	16.40		-	304
0.25	8.4749	1200	5.1367	4.28	16.77	210	28.59	313
		1250		4.69	8.64		-	563
		1300		4.29	16.48		-	288
0.30	8.4660	1200	5.1509	4.18	18.85	270	34.87	298
		1250		4.69	8.90		-	471
		1300		4.11	20.23		-	242

Fig. 5.3 shows that the density increases with increasing Cu^{2+} substitution in

$Mn_{0.50}Zn_{0.50-x}Cu_xFe_2O_4$ up to a certain level (x = 0.10). A possible explanation may be the

formation of solid solution. It is supposed that all Cu^{2+} ions enter into the spinel lattice during sintering and activate the lattice diffusion. This assumption of the formation of solid solution is confirmed by the lattice constant measurement in which the lattice constant decreases with Cu content. The increase of the lattice diffusion usually increases the diffusion path, leading to an increase of the rate of cation interdiffusion in the solid solution which is in agreement with the lattice diffusion mechanism proposed by Gupta and Coble. [3]. After the certain level (x>0.10) density decreases. This decrease in density is attributed to the increased intra-granular porosity resulting from discontinuous grain growth as proposed by Bruke [4]. According to Lange and Kellet [5], grain growth and densification are intimately related. Fig. 5.4 shows the density and porosity of the samples in different temperatures (1200, 1250 and 1300$^{\text{o}}$C). Fig. 5.5 shows that the density of all samples increases with increasing sintering temperature up to 1250$^{\text{o}}$C and then decreases. The increase in density with sintering temperature is expected. This is because during the sintering process, the thermal energy generates a force that drives the grain boundaries to grow over pores, thereby decreasing the pore volume and densifying the material. At higher sintering temperature density is decreased because the intragranular porosity is increased due to discontinuous grain growth. When the grain growth rate is very high, pores may be left behind by rapidly moving grain boundaries, resulting in pores that are trapped inside the grains. The discontinuous growth of the grain rises with temperature and hence contributes toward the reduction of bulk density. Porosity has the opposite trend.
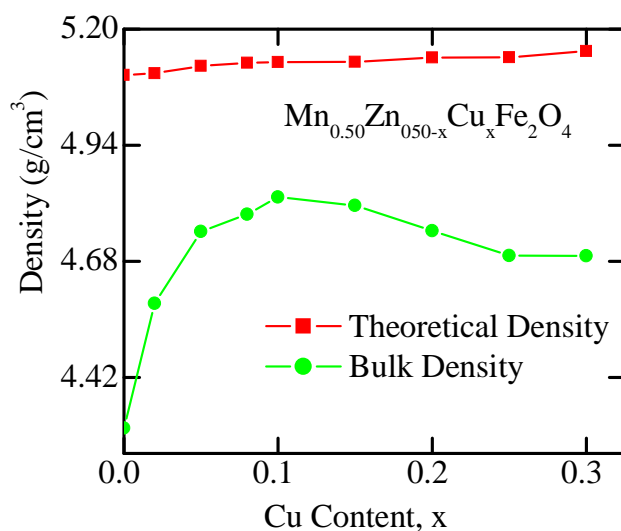
Fig. 5.3. The variation of theoretical density and bulk density with x for $Mn_{0.50}Zn_{0.50-x}Cu_xFe_2O_4$
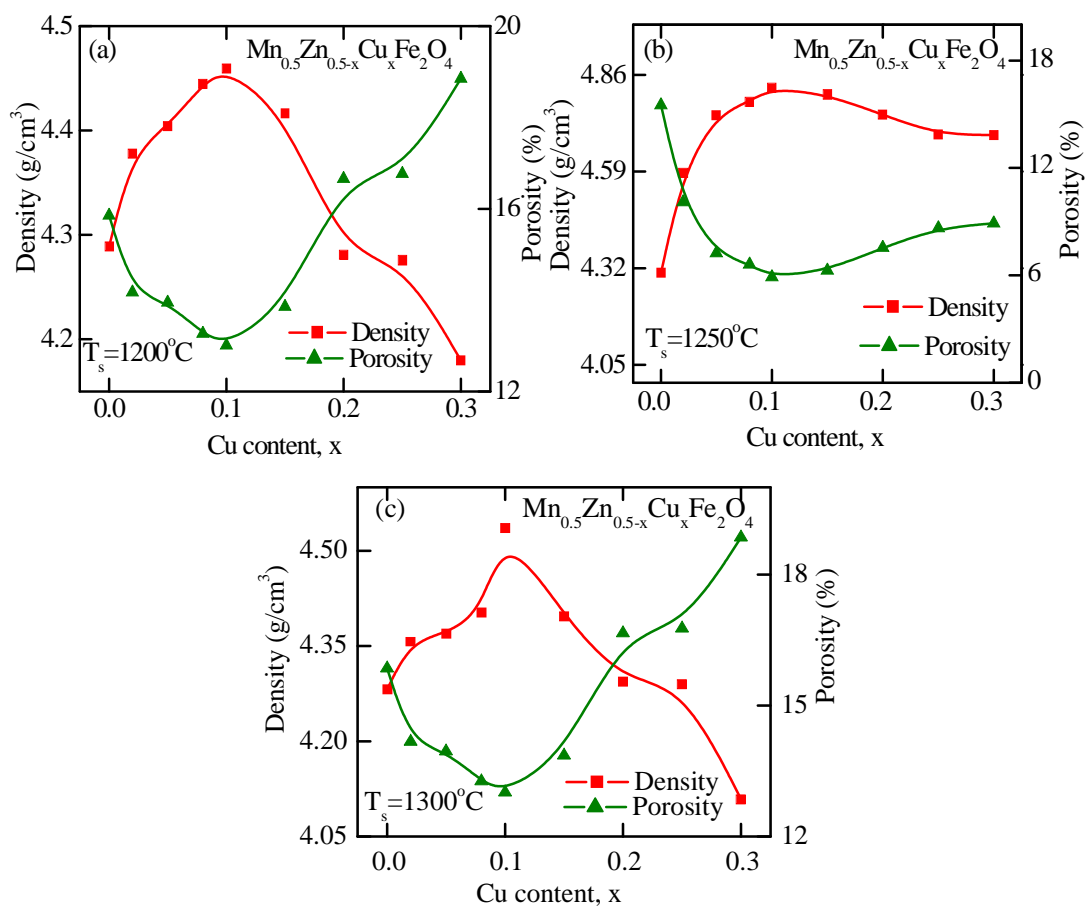
Fig. 5.4. The variation of density and Porosity with x for $Mn_{0.50}Zn_{0.50-x}Cu_xFe_2O_4$ at (a) 1200, (b) 1250 and

(c) 1300°C
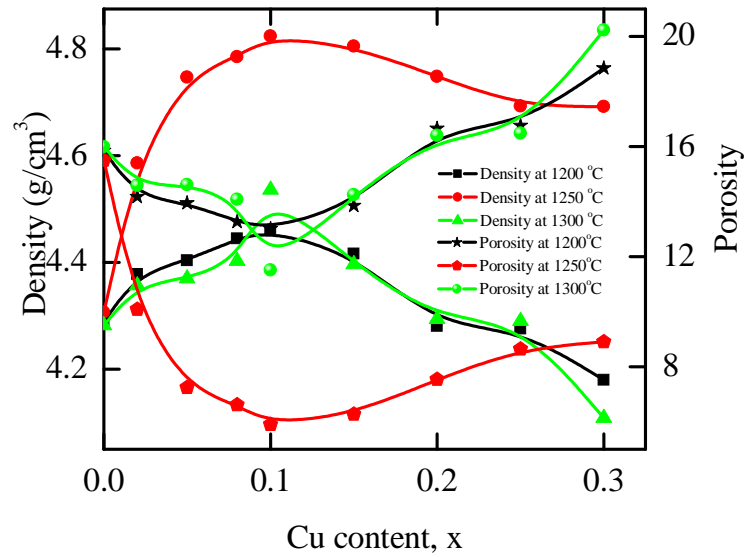
Fig. 5.5. The Variation of density and porosity with various sintering temperature for $Mn_{0.50}Zn_{0.50-x}Cu_xFe_2O_4$

(x = 0.00, 0.02, 0.05, 0.08, 0.10, 0.15, 0.20, 0.25, 0.30)

It is known that the porosity of the ceramic samples results from two sources, intragranular porosity and intergranular porosity. When the grain growth rate is very high, pores may be left behind by rapidly moving grain boundaries, resulting in pores that are trapped inside the grains. This intragranular porosity leads to poor magnetic and mechanical properties. Thus, the total porosity could be written as $P = P_{intra} + P_{inter}$. The intergranular porosity mainly depends on the grain size [6].

5.2 Microstructures of $Mn_{0.50}Zn_{0.50-x}Cu_xFe_2O_4$

The optical micrographs of various $Mn_{0.50}Zn_{0.50-x}Cu_xFe_2O_4$ (x = 0.00, 0.02, 0.05, 0.08. 0.10, 0.15, 0.20, 0.25, 0.30) compositions sintered at 1200°C are shown in Figs. 5.6.
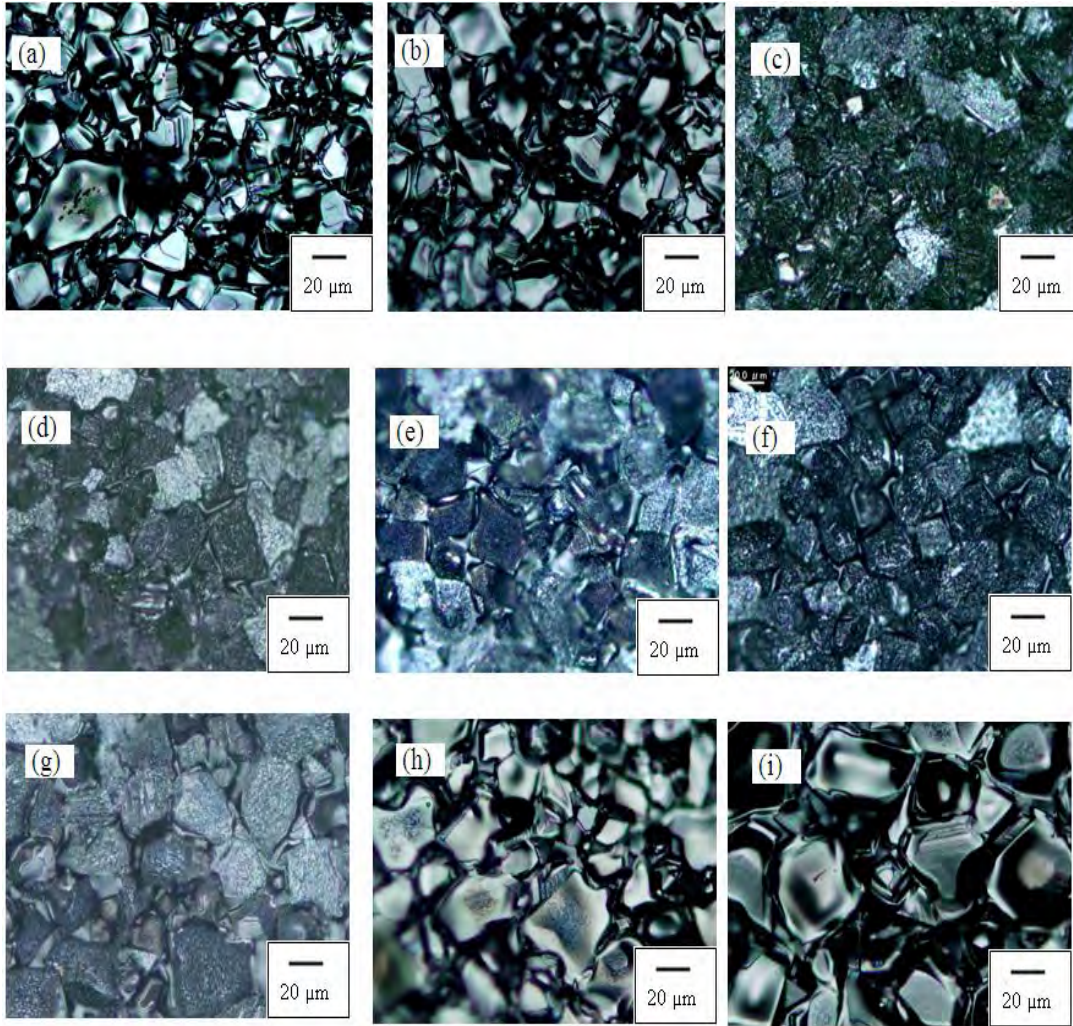
Fig. 5.6. The optical micrographs of $Mn_{0.50}Zn_{0.50-x}Cu_xFe_2O_4$ sintered at temperatures 1200 ^{0}C for (a)x = 0.00, (b) x = 0.02, (c) x = 0.05, (d) x = 0.08, (e) x = 0.10, (f) x = 0.15, (g) x = 0.20, (h) x = 0.25, (i) x = 0.30

From these micrographs it is revealed that *Cu* substitutions have significant influence on microstructures. The average grain size increases with increasing Cu content in the

$Mn_{0.50}Zn_{0.50-x}Cu_xFe_2O_4$. A possible explanation may be the formation of solid solution. It is supposed that all Cu^{2+} ions enter into the spinel lattice during sintering and activate the lattice diffusion. The uniformity and the grain size and the average grain diameter can control properties such as the magnetic permeability. The behavior of grain growth reflects the competition between the driving force for grain boundary movement and the retarding force exerted by pores [7]. During the sintering process, the thermal energy generates a force that drives the grain boundaries to grow over pores, thereby decreasing the pore volume and densifying the material.

5.3 Complex permeability of $Mn_{0.50}Zn_{0.50-x}Cu_xFe_2O_4$

The compositional variation of complex permeability spectra for the $Mn_{0.50}Zn_{0.50-x}Cu_xFe_2O_4$ samples sintered at 1200, 1250, and 1300$^{°}$C are shown in Figs.5.7, 5.8, 5.9, respectively. The initial permeability $\mu_i^{/}$ increase with increasing Cu^{2+} content up to x=0.10, because of increase in density and grain size with Cu^{2+} content. Beyond this value of x, initial permeability decrease with increasing Cu^{2+} content. The general characteristic of the permeability spectra is that the real part of initial permeability $\mu_i^{/}$ remain fairly constant in a certain frequency range, while at higher frequency it drops rapidly to a very small value and there is a increase of imaginary part ($\mu_i^{//}$). The $\mu_i^{//}$ arises due to the lagging of the motion of the domain walls with the applied alternating magnetic field. This behaviour resembles a typical relaxation character. It may be due to reversible displacement of domain walls [8].

$$Mn_{0.50}Zn_{0.50-x}Cu_xFe_2O_4$$
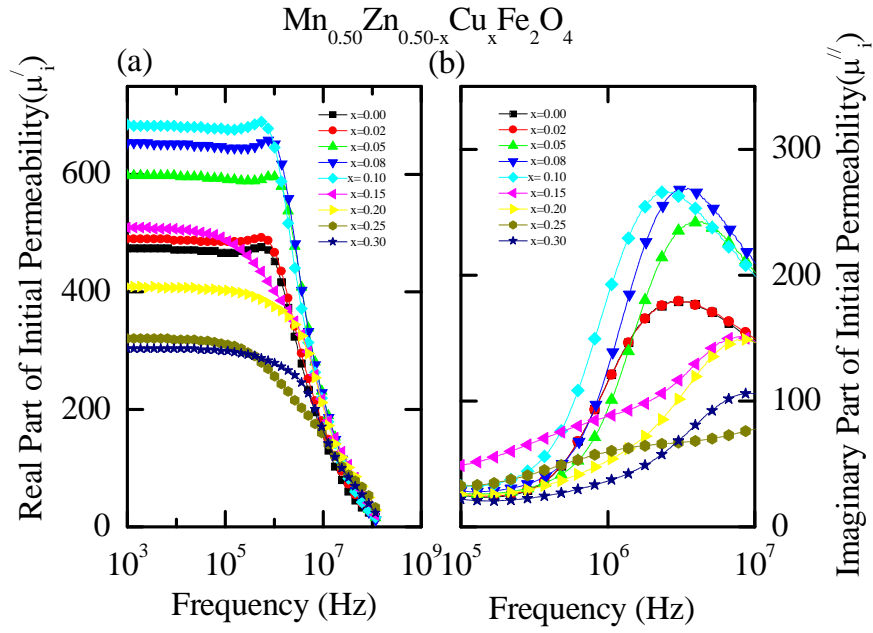
Fig.5.7: (a) The real $\mu_i^{/}$ and (b) imaginary permeability $\mu_i^{//}$ spectra for $Mn_{0.50}Zn_{0.50-x}Cu_xFe_2O_4$ samples

sintered at 1200°C in air.

$$Mn_{0.50}Zn_{0.50-x}Cu_xFe_2O_4$$
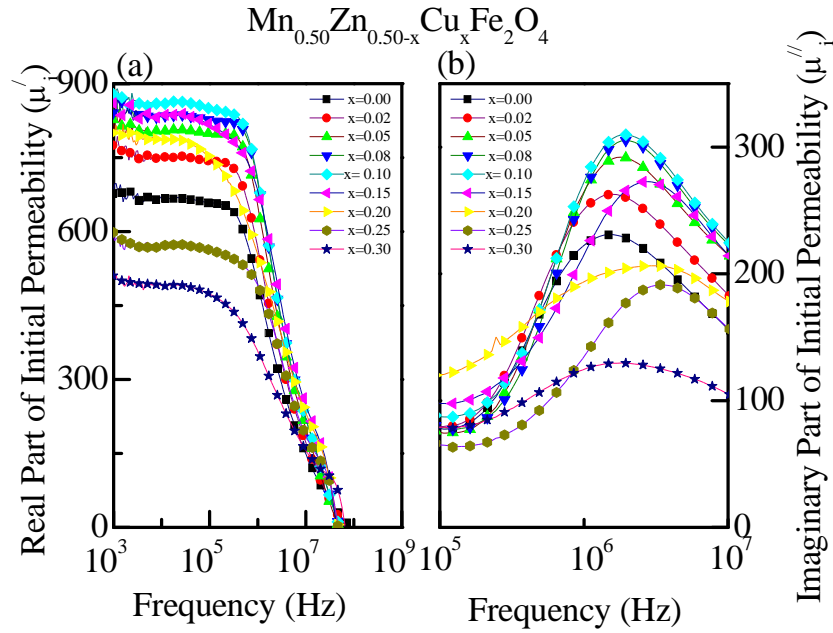
Fig.5.8: (a) The real $\mu_i^{/}$ and (b) imaginary permeability $\mu_i^{//}$ spectra for $Mn_{0.50}Zn_{0.50-x}Cu_xFe_2O_4$ samples

sintered at 1250°C in air.
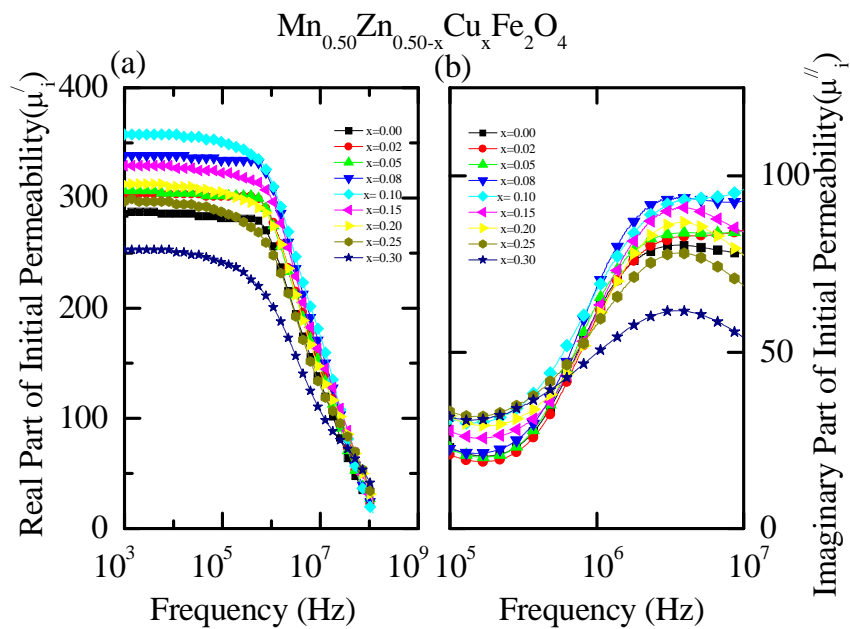
Fig.5.9: (a) The real $\mu_i^{/}$ and (b) imaginary permeability $\mu_i^{//}$ spectra for *Mn$_{0.50}$Zn$_{0.50-x}$Cu$_x$Fe$_2$O$_4$* samples

sintered at 1300˚C in air.
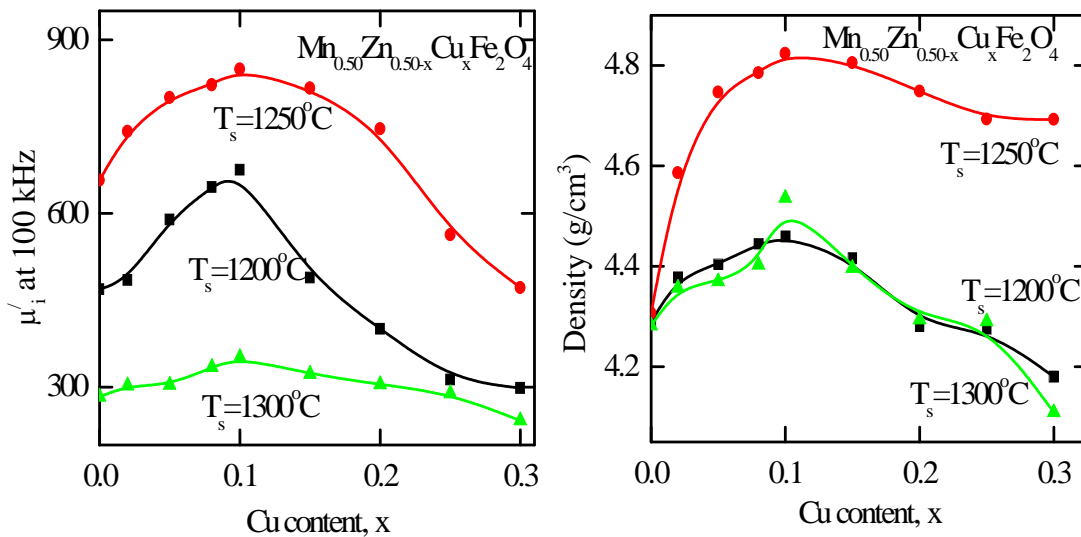
Fig.5.10: The variation of $\mu_i^{/}$ (at 100 kHz) and density with Cu content at various temperatures for

Mn$_{0.50}$Zn$_{0.50-x}$Cu$_x$Fe$_2$O$_4$
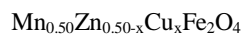
The $\mu_i^/$ increases with increasing sintering temperature because of increase of grain size with temperature. The permeability of polycrystalline ferrite is related to two different magnetizing mechanisms: spin rotation and domain wall motion [9, 10], which can be described as, $\mu_i = 1 + \chi_w + \chi_{spin}$, where χ_w is the domain wall susceptibility, χ_{spin} is intrinsic rotational susceptibility. χ_w and χ_{spin} may be written as: $\chi_w = 3\pi M_s^2 D / 4\gamma$ and $\chi_{spin} = 2\pi M_s^2 / K_u$ with M_s saturation magnetization, K_u the total anisotropy, D the grain size, and γ the domain wall energy. Larger grains tend to consist of a greater number of domain walls. The magnetization caused by domain wall movement requires less energy than that required by domain rotation. As the number of walls increases with the grain sizes, the contribution of wall movement to magnetization is increased. The $\mu_i^/$ is observed highest for sample sintered at 1250 ℃ for all compositions because of the microstructure is homogeneous with large grain size and a uniform size distribution. Also it is found that the sintered density is highest for this temperature. All these values are listed in Table 5.1. Energy loss is an extremely important subject in soft ferrimagnetic materials, since the amount of energy wasted on process other than magnetization can prevent the AC applications of a given material. The ratio of $\mu_i^/$ and $\mu_i^{//}$ representing the losses in the material are a measure of the inefficiency of the magnetic system. Obviously this parameter should be as low as possible. The magnetic losses, which cause the phase shift, can be split up into three components: hysteresis losses, eddy current losses and residual losses. This gives the formula $\tan\delta_m = \tan\delta_h + \tan\delta_e + \tan\delta_r$. The initial permeability μ_i is related to low applied magnetic field. Hysteresis losses vanish at very low field strengths.
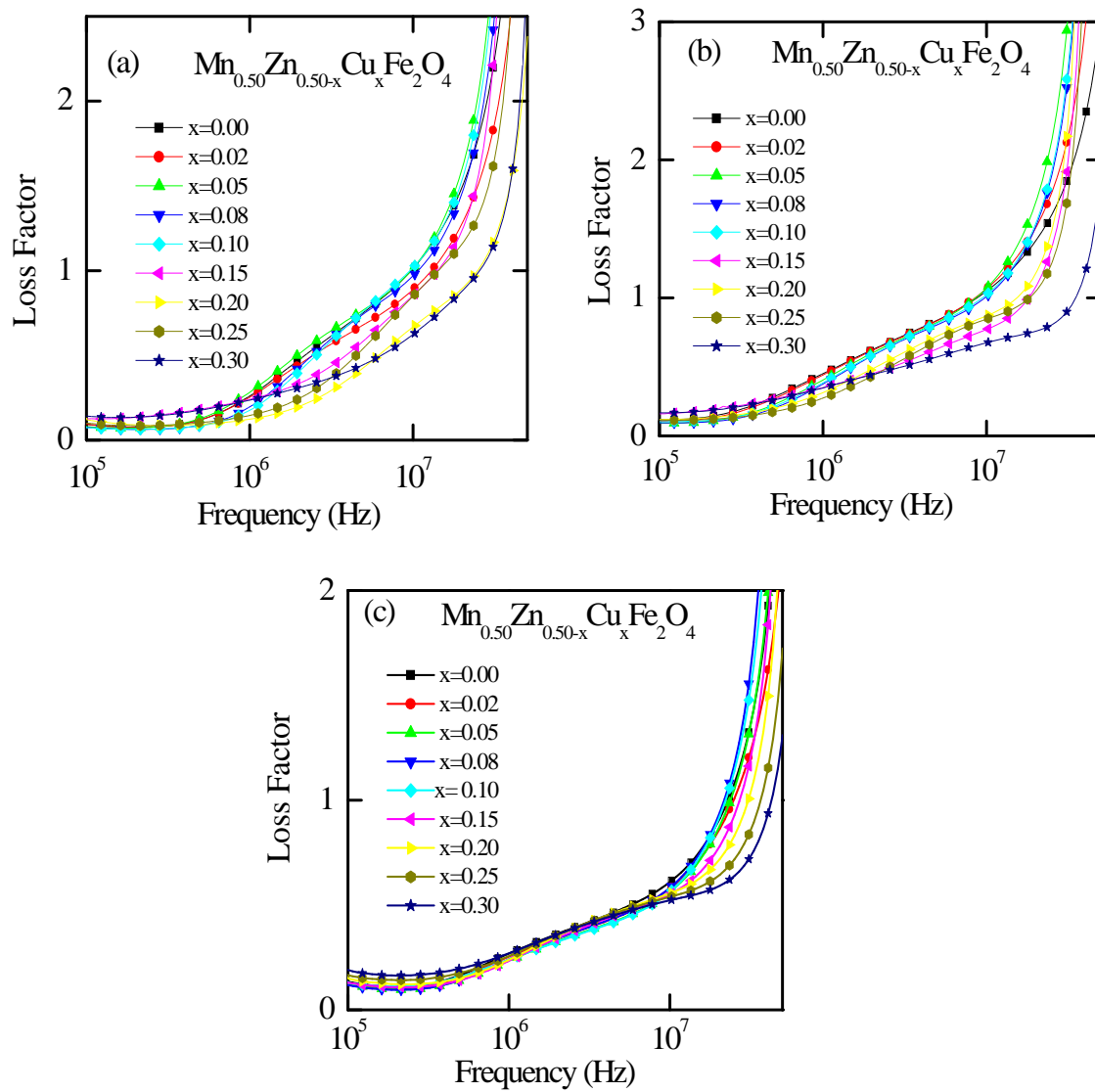
Fig.5.11: The variation of Loss factor with frequency $Mn_{0.50}Zn_{0.50-x}Cu_xFe_2O_4$ samples sintered at (a) 1200 (b) 1250 and (c) 1300°C

Fig. 5.11 shows the variations of loss factors with frequency of different compositions of the samples sintered at different sintering temperature T_s. Loss factors are minimum for frequency up to 1 MHz (depending on compositions and T_s). Thus at low field the remaining magnetic losses are due to eddy current losses and residual losses. Residual losses are independent of frequency. Eddy current losses increase with

frequency and are negligible at very low frequency. Eddy current loss can be expressed as $P_e \approx f^2/\rho$, where P_e is the energy loss per unit volume and ρ is the resistivity [11,12]. To keep the eddy current losses constant as frequency is increased; the resistivity of the material chosen must increase as the square of frequency. The ferrite microstructure is assumed to consist of grains of low resistivity separated by grain boundaries of high resistivity. Thicker grain boundaries are preferred to increase the resistance.
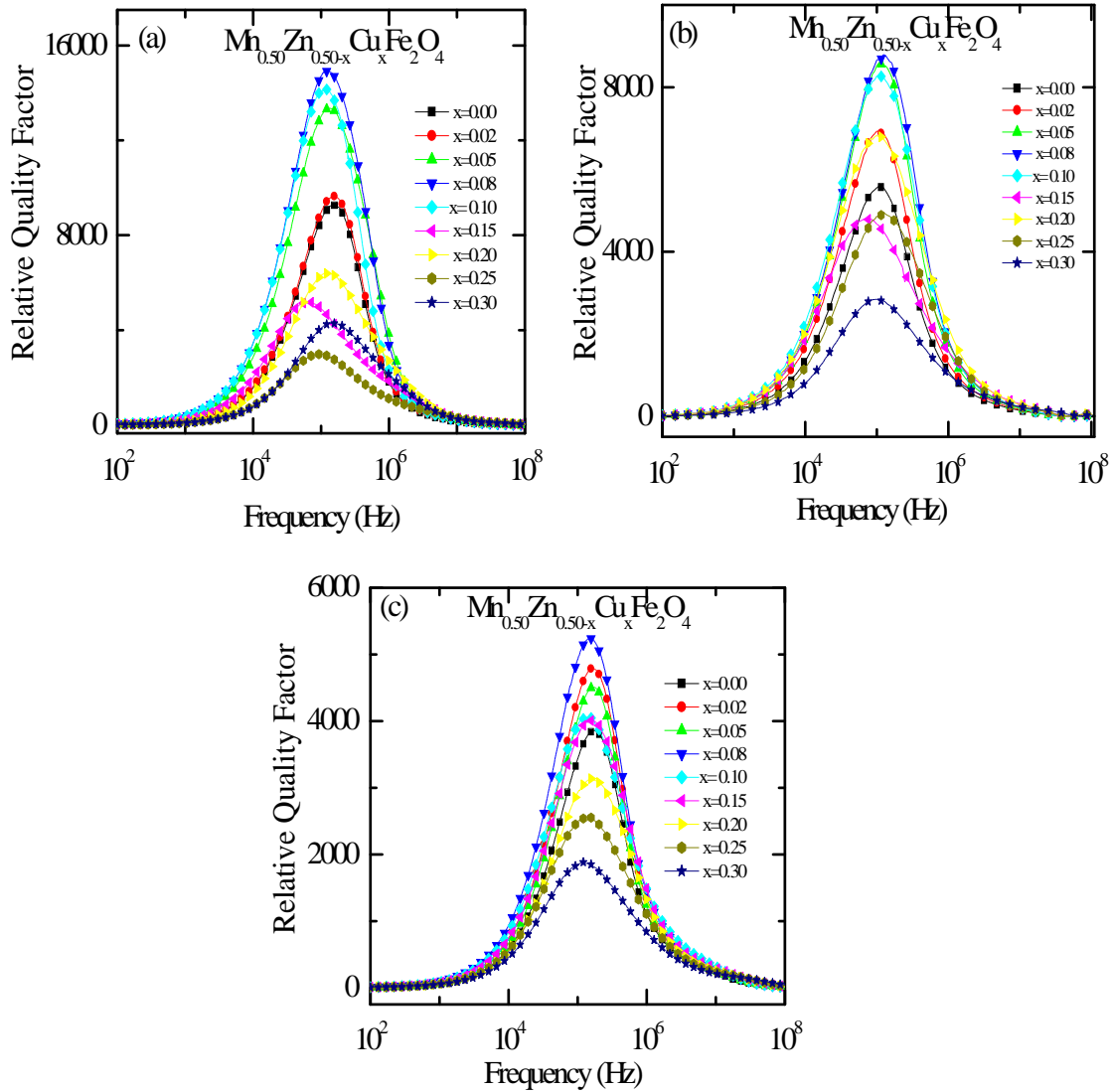
Fig. 5.12: The variation of Quality factor with frequency for $Mn_{0.50}Zn_{0.50-x}Cu_xFe_2O_4$ samples sintered at

(a)   1200 (b) 1250 and (c) 1300 ^{o}C

Relative quality factor (Q factor) for all samples sintered at various temperatures have been calculated from the quality factor and loss factor. Fig. 5.12 shows the variation of Q factor with frequency which reveal that Q-factor increases with an increase of frequency showing a peak and then decrease with further increase of frequency. Highest relative quality factor is obtained by $Mn_{0.50}Zn_{0.42}Cu_{0.08}Fe_2O_4$.

5.4. Temperature-dependent permeability and Néel temperature of

$Mn_{0.50}Zn_{0.50-x}Cu_xFe_2O_4$
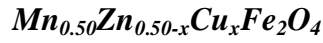
The $\mu_i^/$, as a function of temperature for various $Mn_{0.50}Zn_{0.50-x}Cu_xFe_2O_4$ sintered at 1250 ºC is shown in Fig. 5.13. The $\mu_i^/$ is measured at a constant frequency (100 kHz) of a sinusoidal wave. Permeability falls rapidly when the magnetic state of the ferrite samples changes from ferrimagnetic to paramagnetic. The sharp falling of $\mu_i^/$ with temperature shows the degree of homogeneity [13, 14] of our samples. The Néel temperature, $T_{N,}$ is determined by drawing a tangent for the curve at the rapid decrease of $\mu_i^/$.
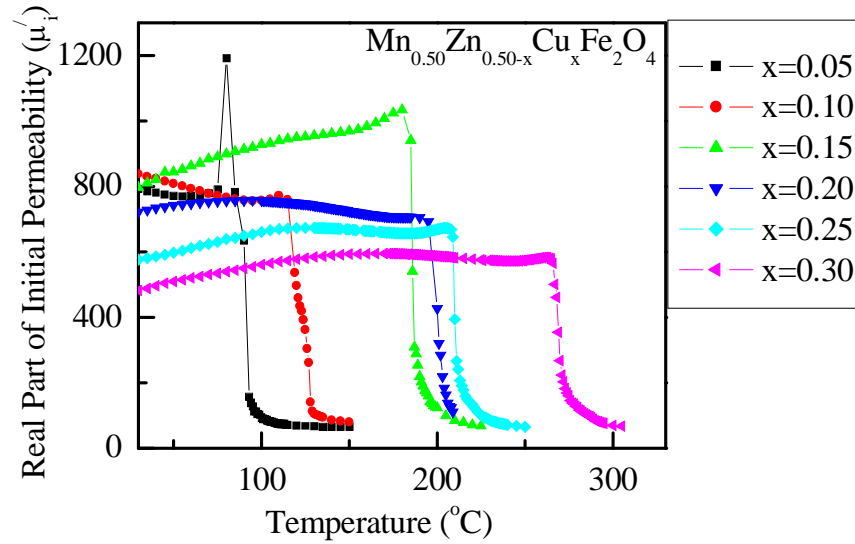
Fig. 5.13: The temperature dependence of $\mu_i^/$ for $Mn_{0.50}Zn_{0.50-x}Cu_xFe_2O_4$ samples sintered at 1250ºC.

The intersection of the tangent with the temperature axis determines T_N. From these curves the T_N's of these samples are determined. It is revealed from Fig. 5.14 that T_N increases as Cu^{2+} increases in $Mn_{0.50}Zn_{0.50-x}Cu_xFe_2O_4$. The T_N for different samples is given in Table-5.1. The increase of the Néel temperature with Cu^{2+} substitution is due to the strengthening of the *A-B* interaction. This could be attributed to the decrease in distance between the moments of *A* and *B* sites, which is confirmed by the decrease in the lattice constant with increasing Cu^{2+} contents. The smallest distance between moments leads the *A-B* interaction to increase for sample $Mn_{0.50}Zn_{0.50-x}Cu_xFe_2O_4$ relative to all other samples and consequently T_N increases.
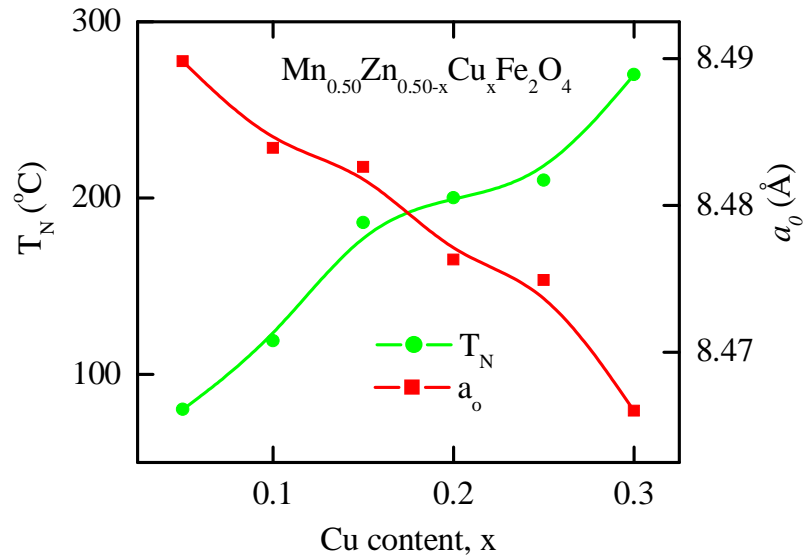
Fig. 5.14: The variation of T_N and a_o with x for various $Mn_{0.50}Zn_{0.50-x}Cu_xFe_2O_4$

Anisotropy constants vary considerably with temperature. In most cases, anisotropy decreases steeply from a high value at low temperature and then slowly decreases down to zero at T_N [11]. There is then no preferred crystallographic direction for the magnetization of a domain. It is observed that the initial permeability, $\mu_i^/$,

increases with temperature to a maximum value just below the T_N. This occurs, because the crystal anisotropy normally decreases with increasing temperature [13]. The initial permeability varies as $\mu_i \approx M_S^2 / K_1^{1/2}$ [11, 16]. Since anisotropy decreases faster than magnetization on heating, the initial permeability expectantly increases with temperature, tends to infinity just below the T_N and then drops for the paramagnetic phase. The peak near T_N is known as the '*Hopkinson*' peak [11].

5.5. DC magnetization of $Mn_{0.50}Zn_{0.50-x}Cu_xFe_2O_4$

The magnetization as a function of applied magnetic field, *M-H*, for various $Mn_{0.50}Zn_{0.50-x}Cu_xFe_2O_4$ samples at room temperature (300K) is shown in Fig. 5.15. The magnetization of all samples increases linearly with increasing the applied magnetic field up to 0.1T. Beyond 0.1T applied field magnetization increases slowly and then saturation occurs. So it is clear that at room temperature all samples are in ferrimagnetic state.
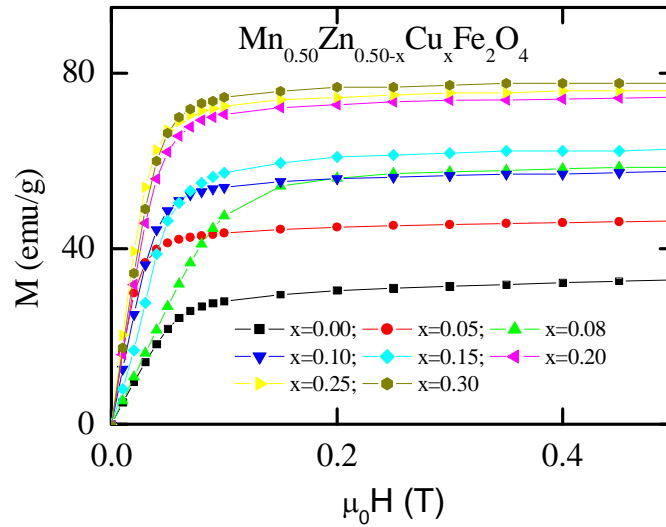
Fig.5.15: The magnetization, *M* versus the applied magnetic field, *H* curves for

$Mn_{0.50}Zn_{0.50-x}Cu_xFe_2O_4$ samples sintered at 1250°C for 5 h in air.

The calculated Bohr magnetons of each composition are enlisted in Table 5.2.

Table 5.2. The saturation magnetization and Bohr magneton of the $Mn_{0.50}Zn_{0.50-x}Cu_xFe_2O_4$ samples sintered at 1250 ^{0}C.

x	Saturation magnetizing field, μ_oH_s (T)	M_s (emu/g)	μ_B (expt)
0.00	0.10	31.66	1.34
0.05	0.10	45.09	1.90
0.08	0.15	56.82	2.40
0.10	0.15	57.09	2.41
0.15	0.15	61.84	2.61
0.20	0.15	73.61	3.11
0.25	0.15	75.27	3.17
0.30	0.15	77.51	3.27
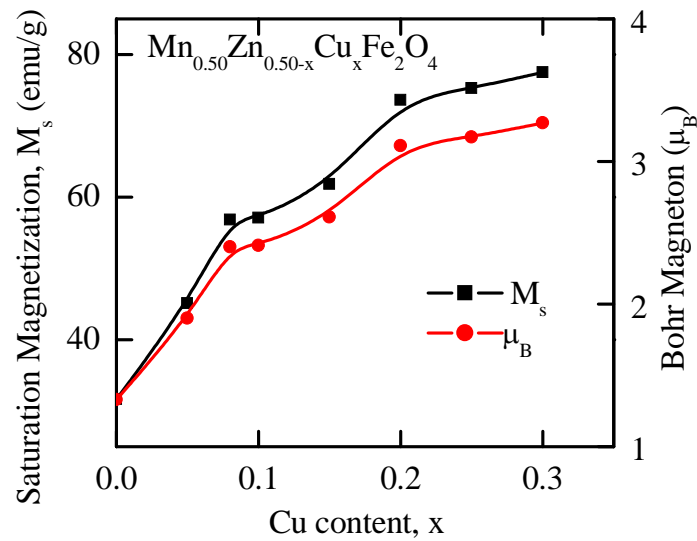
Fig.5.16: The variation of M_s and μ_B with x for $Mn_{0.50}Zn_{0.50-x}Cu_xFe_2O_4$.

Fig. 5.16. shows that magnetization increases with increasing Cu^{2+} content in $Mn_{0.50}Zn_{0.50-x}Cu_xFe_2O_4$. There is strong evidence that Cu^{2+} change to Cu^+ at higher copper concentration [17]. The Cu^+ has a preference to accommodate themselves in A-sites which Cu^+ can force some of Fe^{3+} migrate from A-sites to B-sites. This migration of Fe^{3+} to B-sites will lead to an increase in magnetization in B-sites which leads to the increase of saturation magnetization. This result is expected because there is evidence from the grain size. The magnetization caused by domain wall movement requires less energy than that required by domain rotation. From the microstructures, it is observed that the average grain size increases with increasing Cu contents. From the previous investigations it is observed that domain size is directly proportional to grain size having the relation [18],

Domain Size∞ (Grain size) ^{m}…………………………………………………..(1)

Where m represents parabolic scaling (m =1/2).

The number of domain walls increase with increasing the grain size and so the magnetization.

References

[1]   Hossain, A. K. M. A., Seki, M., Kawai, T. and Tabata, H. "Colossal magnetoresistance in spinel type $Zn_{1-x}Ni_xFe_2O_4$," *J. Appl. Phys.*, **96**, 1273, 2004

[2]   R. D. Shannon *,"Revised Effective Ionic Radii and Systematic Studies of Interatomic Distances in Halides and Chalcogenides",* Acta Crystallographica, A32, Pages 751-767, 1976

.[3]   Gupta, T.K. and Coble, R.L. " Sintering of ZnO: I, Densification and Grain Growth", J. Am. Cream. Soc. 51 (1968) 521.

[4]   Bruke, J. E. in W. D. Kingrey (Ed.), Ceramic Fabrication Processes, Wiley, New York, (1958) 120.

[5]   Lange, R. F., Kellet, B. J., " Thermodynamics of Densification: II, Grain Growth in Porous Compacts and Relation to Densification", J. Am. Ceram. Soc. 72 (1989) 735

[6]   Sattar, A. A., El-Sayed, H. M., El-Shokrofy, K. M. and El-Tabey, M. M., "Improvement of the magnetic properties of Mn-Ni-Zn ferrite by the non-magnetic Al^{3+} ion substitution," *J. Appl. Sci.*, **5**(1)**,** 162 (2005).

[7]   Costa, A. C. F. M., Tortella, E., Morelli, M. R. and Kiminami , R. H. G. A., " Synthesis, microstructure and magnetic properties of Ni-Zn ferrites," *Journal of Magnetism and Magnetic Materials*, **256**, 174 (2003).

[8]   Lebourgeois, R., Ganne, J.P. and Llort, B. "High frequency Mn-Zn power ferrites " J. Phys. IV France 7 Suppl. CI: 105-108 (1997)

[9]   Hu Jun and Yan Mi, "Preparation of high permeability Ni-Cu-Zn ferrite," *Journal of Zhejiang University Science*, **6B**(6), 580 (2005).

[10]   Tsutaoka, T., Ueshima, M., Tokunaga, T., Nakamura, T. and Hatakeyama, K., "Frequency dispersion and temperature variation of complex permeability of Ni-Zn ferrite composite materials," *J. Appl. Phys.*, **78**(6), 3983 (1995).

[11]   Valenzuela, R., *Magnetic Ceramics*, Cambridge University Press, Cambridge (1994).

[12]   Brailsford , F., *Physical Principles of Magnetism*, D. Van Nostrand Company Ltd., London (1966).

[13]   Cullity, B. D., *Introduction to Magnetic Materials*, Addison-Wisley Publishing Company, Inc., California (1972).

[14]   Ocampo, E. J., Rivera, V. and Valenzuela, R., "An apparatus for the measurement of initial magnetic permeability as a function of temperature," *Journal of Physics F: Scientific Instrument*, **13**, 383 (1980).

[15]   Valenzuela, R., "A sensitive method for the determination of the Curie temperature in ferrimagnets," *Journal of Material Science*, **15**, 3137 (1980)

[16]   Ahmed, M. A. and El Hiti, M. A., "Electrical and Dielectric properties of $Zn_{0.8}Co_{0.2}Fe_2O_4$," *J. Phys.*, III France 5, **775** (1995).

[17]   Rahman, I. Z. and Ahmed, T. T., "A study on Cu substituted chemically processed Ni-Zn-Cu ferrites," *J. Magn. Magn. Mater.,* 290-291, 1576-1579, 2005

[18]   Cao, W. and Randal ,C. A., "Grain size and domain size relations in bulk ceramic ferroelectric materials", *J. phys. Chem Solids,* Vol- 57, No.10, pp 1499-1505,1996

CHAPTER 6

CONCLUSIONS

6.1 Conclusions

The XRD patterns for the polycrystalline $Mn_{0.50}Zn_{0.50-x}Cu_xFe_2O_4$ ferrites confirm the formation of spinel structure. Lattice constant, a_o, decreases with increasing of Cu content in various compositions. This phenomenon is explained in terms of ionic radii. Since the ionic radius of Cu^{2+} (0.65Å) is smaller than Zn^{+2}(0.74 Å) therefore, a_o, decreases in $Mn_{0.50}Zn_{0.50-x}Cu_xFe_2O_4$. Since theoretical density depends upon the lattice constant and the molecular weight of the samples, it is observed that the theoretical density of all compositions increases for the decreases of lattice constant in $Mn_{0.50}Zn_{0.50-x}Cu_xFe_2O_4$. Bulk density of all $Mn_{0.50}Zn_{0.50-x}Cu_xFe_2O_4$ ferrites increases and porosity decreases up to the optimum level of Cu content (x = 0.10) and beyond that level density decreases and as well as porosity increases. Bulk density of all $Mn_{0.50}Zn_{0.50-x}Cu_xFe_2O_4$ ferrites increases as the sintering temperature increases from 1200 to 1250°C and beyond this sintering temperature bulk density decreases. On the other hand, porosity decreases with increasing sintering temperature from 1200 to 1250°C and above 1250°C, porosity increases. During the sintering process, the thermal energy generates a force that drives the grain boundaries to grow over pores, thereby decreasing the pore volume and increasing the density of the materials. At higher sintering temperatures the bulk density decreases, because the intragranular porosity increases as a result of discontinuous grain growth which leads to the decrease of the bulk density. The grain size increases with increasing Cu content. It is also noticeable that the average grain size is bigger for $Mn_{0.50}Zn_{0.20}Cu_{0.30}Fe_2O_4.$

The real part of initial permeability, $\mu_i^/$, increases with increasing *Cu* content up to x= 0.10 in *Mn₀.₅₀Zn₀.₅₀₋ₓCuₓFe₂O₄* because the bulk density increases with increasing *Cu* content up to this level. Initial permeability is observed to be maximum for *Mn₀.₅₀Zn₀.₅₀₋ₓCuₓFe₂O₄* ferrites sintered at 1250 $^\circ$C and beyond this sintering temperature $\mu_i^/$ decreases. This can be explained from the density measurement of the studied samples. Maximum density of the samples is found for the sintering temperature 1250 $^\circ$C. Beyond 1250°C, density decreases because of trapped pores inside the grain. These increasing numbers of pores hinder the domain wall motion and cause lower $\mu_i^/$ values for the samples sintered at higher sintering temperature, 1300 $^\circ$C.

The loss factor decreases with the increasing of *Cu* content up to x = 0.08 and increases beyond it. The loss factor increases also with the increase of sintering temperature. From the loss factor we have calculated the relative quality factor for all compositions sintered at various temperatures. It is observed that Q factor increases with increasing *Cu* content up to x= 0.08 and decreases beyond it. It is also observed that Q factor decreases with increasing sintering temperature. For inductors used in filter applications, the quality factor is often used as a measure of performance. The highest *Q* value (14926) is observed for $Mn_{0.50}Zn_{0.42}Cu_{0.08}Fe_2O_4$ ferrite which is probably due to the growth of lesser imperfection.

The T_N increases with increasing *Cu* content in *Mn₀.₅₀Zn₀.₅₀₋ₓCuₓFe₂O₄*. This could be attributed to the decrease in distance between the magnetic moments of tetrahedral A- and the octahedral B-sites which is confirmed by the decrease in the lattice constant with increasing Cu content. Among

$Mn_{0.50}Zn_{0.50-x}Cu_xFe_2O_4$ ferrites, the highest T_N (~270°C) is found for $Mn_{0.50}Zn_{0.2}Cu_{0.3}Fe_2O_4$.

From the *M-H* curves it is clear that at room temperature the polycrystalline $Mn_{0.50}Zn_{0.50-x}Cu_xFe_2O_4$ ferrites are in ferrimagnetic state. The M_s, as well as the μ_B of $Mn_{0.50}Zn_{0.50-x}Cu_xFe_2O_4$, increase with increasing *Cu* content. There is strong evidence that Cu^{2+} change to Cu^+ at higher copper concentration. The Cu^+ has a preference to accommodate themselves in A-sites which Cu^+ can force some of Fe^{3+} migrate from A-sites to B-sites. This migration of Fe^{3+} to B-sites will lead to an increase in magnetization in B-sites which leads to the increase of saturation magnetization. This result is expected because there is evidence from the grain size. The magnetization caused by domain wall movement requires less energy than that required by domain rotation. From the microstructures, it is observed that the average grain size increases with increasing Cu contents. From the previous investigations it is observed that domain size is directly proportional to grain size. So the number of domain walls increase with increasing the grain size which result an enhancement of the magnetization.

LIST OF FIGURES

LIST OF SYMBOLS AND ABBREVIATIONS

AC	Alternating current
B	Magnetic induction
CMR	Colossal magnetoresistance
$F(\theta)$	Nelson-Riley function
f_r	Resonance frequency
g	Landé splitting factor
H_{cr}	Critical field
J	Exchange integral
K	Total anisotropy
K_1	Magnetocrystalline anisotropy constant
L_s	Self-inductance of the sample core
L_o	Inductance of the winding coil without sample
M	Magnetization
M_s	Saturation magnetization
N_A	Avogadro's number
P	Porosity
P_{intra}	Intragranular porosity
P_{inter}	Intergranular porosity
P_e	Eddy-current loss
Q	Relative quality factor
T_c	Curie temperature
T_n	Néel temperature
T_s	Sintering temperature
$tan\delta$	Loss factor
Z	Complex impedance
α	Restoring force coefficient
β	Viscous damping factor
γ	Domain wall energy
ω	Angular velocity
δ_w	Domain wall thickness
μ_i	Initial permeability
μ'	Real part of complex permeability
μ''	Imaginary part of complex permeability
μ_B	Bohr magneton
χ_{spin}	Intrinsic rotational susceptibility
χ_w	Domain wall susceptibility

LIST OF TABLES

CONTENTS

CHAPTER 1

GENERAL INTRODUCTION   1-4

CHAPTER 2

LITERATURE REVIEW   5-39

CHAPTER 3

SAMPLE PREPARATION

CHAPTER 4

EXPERIMENTAL TECHNIQUES

CHAPTER 5

RESULTS AND DISCUSSION

CHAPTER 6

CONCLUSIONS